Citation for final published version:

Buggert, Marcus, Vella, Laura A., Nguyen, Son, Wu, Vincent H., Chen, Zeyu, Sekine, Takuya, Perez-Potti, André, Maldini, Colby R., Manne, Sasikanth, Darko, Samuel, Ransier, Amy, Kuri-Cervantes, Leticia, Japp, Alberto Sada, Brody, Irene Bukh, Ivarsson, Martin A., Gorin, Jean-Baptiste, Rivera-Ballesteros, Olga, Hertwig, Laura, Antel, Jack P., Johnson, Matthew E., Okoye, Afam, Picker, Louis, Vahedi, Golnaz, Sparrelid, Ernesto, Llewellyn-Lacey, Sian, Gostick, Emma, Sandberg, Johan K., Björkström, Niklas, Bar-Or, Amit, Dori, Yoav, Naji, Ali, Canaday, David H., Laufer, Terri M., Wells, Andrew D., Price, David A. ORCID: https://orcid.org/0000-0001-9416-2737, Frank, Ian, Douek, Daniel C., Wherry, E. John, Itkin, Maxim G. and Betts, Michael R. 2020. The identity of human tissue-emigrant CD8+ T cells. Cell 183 (7) , pp. 1946-1961. 10.1016/j.cell.2020.11.019 file

Publishers page: http://dx.doi.org/10.1016/j.cell.2020.11.019 <http://dx.doi.org/10.1016/j.cell.2020.11.019>

The identity of human tissue-emigrant CD8$^+$ T cells

Marcus Buggert[1,2,3], Laura A. Vella[3,4], Son Nguyen[2,3], Vincent Wu[2,3], Zeyu Chen[3,5], Takuya Sekine[1], André Perez-Potti[1], Colby R. Maldini[2,3], Sasikanth Manne[2,3], Samuel Darko[6], Amy Ransier[7], Leticia Kuri-Cervantes[2,3], Alberto Sada Japp[2,3], Irene Bukh Brody[2,3], Martin A. Ivarsson[1], Jean-Baptiste Gorin[1], Olga-Rivera Ballesteros[1], Laura Hertwig[1], Jack P. Antel[8], Matthew E. Johnson[9,10], Afam Okoye[11], Louis Picker[11], Golnaz Vahedi[3,12], Ernesto Sparrelid[13], Sian Llewellyn-Lacey[14], Emma Gostick[14], Johan Sandberg[1], Niklas Björkström[1], Amit Bar-Or[2,8,15,16], Yoav Dori[17], Ali Naji[2,18], David H. Canaday[19,20], Terri M. Laufer[3,21,22], Andrew D. Wells[3,10,23], David A. Price[14,24], Ian Frank[25], Daniel C. Douek[6], E. John Wherry[3,5,26], Maxim G. Itkin[27], Michael R. Betts[2,3]

[1]Center for Infectious Medicine, Department of Medicine Huddinge, Karolinska Institutet, Karolinska University Hospital Huddinge, Stockholm, Sweden

[2]Department of Microbiology, Perelman School of Medicine, University of Pennsylvania, Philadelphia, PA, USA

[3]Institute for Immunology, Perelman School of Medicine, University of Pennsylvania, Philadelphia, PA, USA

[4]Division of Infectious Diseases, Children's Hospital of Philadelphia, Philadelphia, PA, USA

[5]Department of Systems Pharmacology and Translational Therapeutics, University of Pennsylvania, Philadelphia, PA, USA

[6]Human Immunology Section, Vaccine Research Center, National Institute of Allergy and Infectious Diseases, National Institutes of Health, Bethesda, MD, USA

[7]Genome Analysis Core, Vaccine Research Center, National Institute of Allergy and Infectious Diseases, National Institutes of Health, Bethesda, MD, USA

[8]Neuroimmunology Unit, Montreal Neurological Institute, McGill University, Montreal, QC, Canada

[9]Division of Human Genetics, Children's Hospital of Philadelphia, Philadelphia, PA, USA

[10]Center for Spatial and Functional Genomics, Children's Hospital of Philadelphia, Philadelphia, PA, USA

[11]Vaccine and Gene Therapy Institute and Oregon National Primate Research Center, Oregon Health & Science University, Beaverton, OR, USA

[12]Department of Genetics, Perelman School of Medicine, University of Pennsylvania, Philadelphia, PA, USA
[13]Division of Surgery, Department of Clinical Science, Intervention and Technology, Karolinska Institutet, Stockholm, Sweden
[14]Division of Infection and Immunity, Cardiff University School of Medicine, Cardiff, UK
[15]Center for Neuroinflammation and Experimental Therapeutics, Perelman School of Medicine, University of Pennsylvania, Philadelphia, PA, USA
[16]Department of Neurology, Perelman School of Medicine, University of Pennsylvania, Philadelphia, PA, USA
[17]Division of Cardiology, Department of Pediatrics, Children's Hospital of Philadelphia, Philadelphia, PA, USA
[18]Department of Surgery, Perelman School of Medicine, University of Pennsylvania, Philadelphia, PA, USA
[19]Division of Infectious Diseases and HIV Medicine, Case Western Reserve University, Cleveland, OH, USA
[20]Geriatric Research, Education and Clinical Center, Louis Stokes VA Medical Center, Cleveland, OH, USA
[21]Department of Medicine, Perelman School of Medicine, University of Pennsylvania, Philadelphia, PA, USA
[22]Department of Medicine, Corporal Michael J Crescenz VA Medical Center, Philadelphia, PA, USA
[23]Department of Pathology and Laboratory Medicine, Children's Hospital of Philadelphia, Philadelphia, PA, USA
[24]Systems Immunity Research Institute, Cardiff University School of Medicine, Cardiff, UK
[25]Division of Infectious Diseases, Perelman School of Medicine, University of Pennsylvania, Philadelphia, PA, USA
[26]Parker Institute for Cancer Immunotherapy, University of Pennsylvania, Philadelphia, PA, USA
[27]Center for Lymphatic Disorders, Department of Radiology, Perelman School of Medicine, University of Pennsylvania, Philadelphia, PA, USA

Correspondence: Marcus Buggert (marcus.buggert@ki.se) or Michael R. Betts (betts@pennmedicine.upenn.edu).

ABSTRACT

Lymphocyte migration is essential for adaptive immune surveillance. However, our current understanding of this process is rudimentary, because most human studies to date have been restricted to immunological analyses of blood and various tissues. We used an integrated approach to characterize tissue-emigrant immune cells in thoracic duct lymph (TDL). The prevalent immunocytes in human and non-human primate efferent lymph were T cells. Cytolytic CD8$^+$ T cell subsets with effector-like epigenetic and transcriptional signatures were clonotypically discrete and selectively confined to the intravascular circulation, whereas non-cytolytic CD8$^+$ T cell subsets with stem-like epigenetic and transcriptional signatures predominated in tissues and TDL. Moreover, these anatomically distinct gene expression profiles were recapitulated at the level of individual clonotypes, suggesting parallel differentiation programs independent of the expressed antigen receptor. Our collective dataset provides an atlas of the migratory immune system and defines the nature of tissue-emigrant CD8$^+$ T cells that recirculate via TDL.

INTRODUCTION

The pioneering work of Gowans and colleagues taught us that lymphocytes egress continuously from peripheral tissues and lymph nodes (LNs) and return to the intravascular circulation in a unidirectional manner via the lymphatic system (Gowans, 1957, 1959; Gowans and Knight, 1964). This process of lymphocyte migration now underpins the concept of immune surveillance. The thoracic duct is the major anatomical structure that carries terminal efferent lymph to the blood stream, draining the entire subdiaphragmatic compartment and the upper left part of the body (Phang et al., 2014). A vast majority of immune cells therefore egress from lymphoid tissues (LTs) and non-lymphoid tissues (NLTs) into the thoracic duct (Kubik, 1973). Although it has been estimated that up to 3 x 10^{10} immune cells migrate daily via this route (Pabst, 1988), current knowledge is based primarily on animal studies, and the nature of lymphocyte subsets that egress from human tissues has remained obscure (Buggert et al., 2018; Fox et al., 1984; Girardet and Benninghoff, 1977; Lemaire et al., 1998; Vella et al., 2019; Voillet et al., 2018).

A series of elegant studies in rats and sheep between the 1960s and the 1980s reported that thoracic duct lymph (TDL) was composed mainly of T cells (Gowans, 1957; Mackay et al., 1988; Mackay et al., 1990; Maddox et al., 1985). Most of the cells in these models exhibited a naive phenotype and entered the efferent lymphatic system from LNs via high endothelial venules (Hall and Morris, 1965; Mackay et al., 1990; Mackay et al., 1992; Smith et al., 1970). Memory T cells were subsequently categorized into two major subsets, namely central memory T (T_{CM}) cells, which proliferative vigorously in response to activation and express the LT-homing receptors CCR7 and CD62L, and effector memory T (T_{EM}) cells, which are fully equipped with effector capabilities and traffick to NLTs (Sallusto et al., 1999). However, this binary classification was based on studies of intravascular lymphocytes, and more recent work has suggested greater complexity, including the existence of a T_{EM}-like subset that expresses intermediate levels of CX3CR1 and patrols NLTs (Gerlach et al., 2016).

The early studies in rats by Gowans and colleagues suggested that the number of lymphocytes migrating via the thoracic duct on a daily basis was sufficient to replace the entire intravascular pool multiple times, and a later study in humans estimated this exchange rate at 48 times per day (Schick et al., 1975). However, these estimates were based on various labeling methods designed to track lymphocytes from the thoracic duct or the dilution of isotopes among intravascular lymphocytes, which do not account for the possible existence of lymphocyte populations that remain in the blood and do not recirculate via LTs or NLTs. The concept that all human T cells recirculate has also been challenged by the identification of tissue-resident memory T (T_{RM}) cells (Gebhardt et al., 2009; Masopust et al., 2010; Masopust et al., 2001; Wakim et al., 2008), which form highly stable populations in solid tissues (Buggert et al., 2019; Szabo et al., 2019). T_{RM} cells dominate the total pool of memory $CD8^+$ T cells in NLTs (Steinert et al., 2015) and generate immediate effector responses after secondary challenge (Gebhardt et al., 2009). The protection afforded by T_{RM} cells is thought to involve cytolytic activity (Masopust et al., 2001), because many murine T_{RM} cells constitutively express the serine protease granzyme B (GzmB) (Masopust et al., 2006). However, this paradigm does not necessarily apply to all human T_{RM} cells (Bartolome-Casado et al., 2019; Buggert et al., 2018; Pallett et al., 2017), which exhibit heterogeneous transcriptional profiles (Kumar et al., 2017) and are thought to work partly as innate-like sensors (Schenkel et al., 2013).

To address these knowledge gaps, we characterized the tissue-emigrant immune system in humans and non-human primates. In contrast to prevalent models of lymphocyte trafficking in LTs and NLTs, our data show that cytolytic memory $CD8^+$ T cells are confined to the intravascular circulation under homeostatic conditions, whereas stem-like memory $CD8^+$ T cells survey tissues and recirculate via TDL.

RESULTS

Immunological atlas of human TDL

Current knowledge of the thoracic duct immune system derives primarily from older studies with limited human replicates (Fox et al., 1984; Girardet and Benninghoff, 1977; Lemaire et al., 1998). These studies also lacked the technology required to profile the functional, phenotypic, and transcriptional properties of immune cell subpopulations. We therefore set up a research protocol to acquire matched blood and TDL from a large cohort of individuals (n = 210) with clinical indications for undergoing thoracic duct cannulation. A total of 52 of these individuals between the ages of 3 months and 88 years participated in this study (Table S1).

We first defined the major hematopoietic cell subsets in paired samples of blood and TDL (Figure 1A and Figure S1A). The majority of immune lineage cells ($CD45^+$) in TDL were T cells (75%) or B cells (20%) (Figure 1B). Lower frequencies of innate lymphoid cells (ILCs) and higher frequencies of granulocytes, monocytes, dendritic cells (DCs), and hematopoietic stem cells (HSCs) were present in blood versus TDL (Figures 1B and S1B). Natural killer (NK) cells were present at similar frequencies in each compartment (Figures 1B and S1B). A direct correlation was observed between the frequency of neutrophils and the relative frequency of red blood cells in TDL (Figure S1C). Blood contamination therefore likely explained the occasional detection of neutrophils in TDL.

Highly differentiated $CD8^+$ T cells are uncommon in TDL

To extend these findings, we compared the general memory characteristics of $CD8^+$ T cells in blood versus TDL based on the expression of CCR7, CD27, and CD45RA (Figure S2A). This analysis revealed that T_{EM} and terminally differentiated effector memory T (T_{EMRA}) cells predominated in blood, whereas naive and T_{CM} cells predominated in TDL (Figure 2A). A similar pattern was observed in rhesus macaques based on the expression of CD28 and CD95 (Figure 2B) or CCR7 and CD95 (Figure S2B).

In more detailed flow cytometric analyses, we found that memory $CD8^+$ T cells more commonly expressed certain integrins (CD103), chemokine receptors (CCR5, CXCR3, and CXCR5), and early differentiation markers (CD27 and CD127) in TDL versus blood and more commonly expressed late differentiation and effector markers (CD57, CX3CR1, and KLRG-1) in blood versus TDL (Figure 2C). Hierarchical clustering using these and other markers revealed that each memory $CD8^+$ T cell subset exhibited unique phenotypic characteristics in various lymphoid organs, including tonsils, iliac LNs, and mesenteric LNs (Figure 2D). These clusters were distinguished by the expression of CD69, likely indicating residency in LTs (Buggert et al., 2018). In contrast, T_{EM} and T_{EMRA} cells in blood formed a discrete cluster, whereas T_{CM} cells in blood clustered with all memory subsets in TDL (Figure 2D). Principal component analysis (PCA) confirmed that T_{EM} and T_{EMRA} cells in blood segregated away from other memory clusters (Figure 2E), driven largely by the expression CD25, CD57, CX3CR1, and KLRG1 (Figure 2F). This result was further corroborated via an in-depth analysis of naive and memory $CD8^+$ T cell subsets defined using the core markers CCR7, CD27, CD45RA, and CD95 (Figure S2C). Merged t-distributed stochastic neighbor embedding (tSNE) analysis further showed that $CCR7^-$ memory $CD8^+$ T cells in blood often lacked CD27 and CD127 and commonly expressed markers associated with late differentiation, whereas $CCR7^-$ memory $CD8^+$ T cells in TDL mostly expressed CD27 and CD127 (Figure 2G and S2D).

Collectively, these analyses demonstrated that naive and early memory $CD8^+$ T cells were selectively enriched in TDL and that late memory $CD8^+$ T cells, defined according to standard markers, were more differentiated in blood versus TDL.

Effector memory $CD8^+$ T cells exhibit stem-like signatures in TDL

To determine the transcriptional basis of these phenotypic differences, we performed an extensive RNA-sequencing (RNA-seq) analysis of naive and memory $CD8^+$ T cell subsets in blood, TDL, and mesenteric LNs (Figure 3A). A tSNE representation of these transcriptomes revealed that T_{CM} cells in blood clustered in close proximity with all memory subsets in TDL (Figure 3A). In contrast, T_{EM} and T_{EMRA} cells in blood clustered away from all other memory subsets, including T_{EM} and T_{EMRA} cells in TDL and mesenteric LNs (Figure 3A). We also identified a core signature of genes that were differentially expressed between T_{EM} and T_{EMRA} cells in blood versus TDL (fold change > 2; $p < 0.05$) (Table S2 and S3). Genes encoding cytolytic and effector molecules (*Gzmb*, *Gzmh*, *Cx3cr1*, *Prss23*, and *Spon2*) were upregulated among T_{EM} and T_{EMRA} cells in blood, whereas trafficking (*Ccr2*, *Ccr4*, *Ccr9*, *Itga1*, *Itga4*, *Itgb7*, and *S1pr4*) and self-renewal genes (*Tcf7*, *Il7r*, *Cd27*, *Cd28*, and *Nell2*) were upregulated among T_{EM} and T_{EMRA} cells in TDL (Figure 3B). Gene set enrichment analysis (GSEA) confirmed that signatures associated with cytolytic activity, degranulation, and differentiation were enriched among T_{EM} and T_{EMRA} cells in blood and further showed that signatures associated with cell cycle transition and telomere maintenance were enriched among T_{EM} and T_{EMRA} cells in TDL (Figure 3C).

In further experiments, we used single-cell RNA-seq (scRNA-seq) to compare the gene expression profiles of memory CD8$^+$ T cells in matched samples of blood and TDL (Figure 3D). Dimensionality reduction via Uniform Manifold Approximation and Projection (UMAP) revealed an effector-like gradient (Cano-Gamez et al., 2020) that progressively spanned clusters with gene expression profiles resembling naive, T_{CM}, T_{EM}, and T_{EMRA} cells (Figure 3D). Memory CD8$^+$ T cells in blood were enriched for T_{EMRA}-like clusters, characterized by relative overexpression of the effector-related genes *Gzmb*, *Prf1*, *Cx3cr1*, *Znf683*, *Tox*, and *Tbx21*, whereas memory CD8$^+$ T cells in TDL were enriched for naive-like, T_{CM}-like, and T_{EM}-like clusters, characterized by relative overexpression of the early differentiation genes *Tcf7*, *Cd27*, *Il7r*, *Ccr7*, *Sell*, and *Gzmk* (Figure 3D and 3E). Moreover, the T_{EM}-like and T_{EMRA}-like clusters in blood were transcriptionally comparable to previously reported effector-like datasets, whereas the T_{EM}-like and T_{EMRA}-like clusters in TDL were enriched for gene signatures associated with ribosome biogenesis (Figure 3F), which could potentially impact mRNA translation (Nguyen et al., 2019).

Flow cytometric analyses confirmed that memory CD8$^+$ T cells in TDL lacked the cytolytic proteins GzmB and perforin in humans (Figure 3G) and rhesus macaques (Figure S2E). In contrast, TCF-1, a transcription factor expressed by memory T cells with stem cell-like properties (Jeannet et al., 2010; Utzschneider et al., 2016; Zhou et al., 2010), was detected at lower frequencies among T_{EM} and T_{EMRA} cells in blood versus TDL (Figure 3H). A discrepant pattern was also observed for the T-box binding transcription factors Eomes and T-bet (Figure 3I). Specifically, Eomes^{hi}T-bet^{lo} T_{EM} and T_{EMRA} cells predominated in TDL, whereas Eomes^{lo}T-bet^{hi} T_{EM} and T_{EMRA} cells predominated in blood and were virtually absent in TDL (Figure 3I). Memory CD8$^+$ T cells in rhesus macaques similarly expressed T-bet at much higher frequencies in blood versus TDL (Figure S2F). In line with these results, cytolytic activity was largely confined to intravascular CD8$^+$ T cells and correlated directly with expression levels of GzmB and perforin (Figure 3J). Moreover, CD8$^+$ T_{EM} and T_{EMRA} cells isolated from blood upregulated GzmB and perforin after stimulation with phorbol myristate acetate (PMA) and ionomycin, unlike CD8$^+$ T_{EM} and T_{EMRA} cells isolated from TDL, which instead upregulated interleukin (IL)-2 at levels equivalent to those observed among CD8$^+$ T_{CM} cells isolated from blood and TDL (Figure 3K).

Collectively, these data further indicated that tissue-emigrant CCR7$^-$ memory CD8$^+$ T cells were less differentiated than intravascular CCR7$^-$ memory CD8$^+$ T cells.

Effector memory CD8$^+$ T cells are epigenetically distinct in blood and TDL

The data presented thus far suggested that cytolytic CD8$^+$ T$_{EM}$ and T$_{EMRA}$ cells were confined to the intravascular compartment. However, it remained possible that dynamic changes in gene and protein expression allowed these cells to access tissue sites and recirculate via TDL. We therefore used the Assay of Transposase Accessible Chromatin Sequencing (ATAC-seq) to profile the open chromatin landscape of CD8$^+$ T$_{EM}$ and T$_{EMRA}$ cells in blood, TDL, and mesenteric LNs (Figure 4A). Such epigenetic signatures are relatively stable and track prior imprints of differentiation. Global chromatin accessibility was compared among distinct cell subsets via PCA. This analysis revealed that T$_{EM}$ and T$_{EMRA}$ cells in TDL colocalized separately from T$_{EM}$ and T$_{EMRA}$ cells in blood and mesenteric LNs (Figure 4A). Certain transcription factor family motifs, most notably T-bet (TBOX) and RUNX, were enriched among T$_{EM}$ and T$_{EMRA}$ cells in blood versus TDL (Figure 4B). Likewise, specific open chromatin regions (OCRs) and motif families (RUNX, bZIP, and bHLH) next to effector genes (*Gzmh*, *Gzmb*, *Tbx21*, and *Prf1*) were more accessible among T$_{EM}$ and T$_{EMRA}$ cells in blood versus TDL (Figure 4C). In additional experiments, we incubated peripheral blood mononuclear cells (PBMCs) and TDL mononuclear cells (TDLMCs) with plasma or TDL to exclude the possibility that soluble factors could regulate the expression of cytolytic molecules, exemplified by GzmB. No upregulation of GzmB was observed in either compartment under either of these conditions (Figure S2G).

Collectively, these results indicated that effector memory CD8$^+$ T cell subsets were characterized by distinct open-chromatin structures in blood versus TDL.

Cytolytic and non-cytolytic CD8$^+$ T cells are clonotypically divergent

To seek further evidence of divergent maturational pathways, we used an unbiased molecular approach to sequence T cell receptor (TCR) β gene (*TRB*) rearrangements (TCR-seq) expressed among memory CD8$^+$ T cell subsets in blood and TDL. Pilot experiments revealed the presence of cytolytic precursors and cytolytic effectors in the T$_{EM}$ and T$_{EMRA}$ subsets (Figure S3A), consistent with previous work (Patil et al., 2018). We therefore used CX3CR1 as a surrogate marker to identify cytolytic effector CD8$^+$ T cells (Figure 5A; (Bottcher et al., 2015). As insufficient numbers of CX3CR1$^+$ cells were present in TDL (Figures 5A, S3B, and

S3C), we compared CCR7$^-$ memory CX3CR1$^+$ cells in blood with CCR7$^+$ memory CX3CR1$^-$ (*i.e.*, predominantly T$_{CM}$) and CCR7$^-$ memory CX3CR1$^-$ (*i.e.*, predominantly T$_{EM}$) cells in blood and TDL (Figure 5B). Repertoire diversity was substantially lower among CCR7$^-$ memory CX3CR1$^+$ cells in blood versus all other memory subsets in blood and TDL (Figure 5C). A near-perfect correlation was observed between the frequencies of T$_{CM}$ clonotypes in blood and TDL, indicating that T$_{CM}$ cells in blood were highly representative of T$_{CM}$ cells that egressed from tissues and recirculated via TDL (Figures 5D and 5E). In contrast, limited clonotypic overlap was observed between the T$_{EM}$ subsets in blood and TDL, and the cytolytic effector repertoires were hierarchically dissimilar from all other memory subsets in blood and TDL (Figures 5D and 5E).

Cytolytic CD8$^+$ T cells are selectively retained in the intravascular circulation

To determine if cytolytic CD8$^+$ T cells were present in tissues, we collected unpaired human LTs (tonsils and mesenteric LNs) and NLTs (colon, decidua, and liver). Cytolytic CD8$^+$ T cells were common in blood and rare in all other anatomical locations (Figure 6A). Non-resident CD8$^+$ T cells (CD69$^-$) were predominantly CCR7$^+$ in LTs and CCR7$^-$ in NLTs (Figure 6B), consistent with previous work (Sallusto et al., 1999). Most non-resident CD8$^+$ T$_{EM}$ cells in the decidua also lacked CX3CR1 (Figure 6C; (Gerlach et al., 2016). In addition, we collected matched samples of blood entering the liver via the portal vein and leaving the liver via the central hepatic veins. Similar frequencies of non-resident cytolytic CD8$^+$ T cells (CD57$^+$) were present before and after organ transit (Figure S5D). These results were confirmed using matched samples of arterial and venous blood from other donors (Figure S5E).

To investigate the migratory capabilities of cytolytic CD8$^+$ T cells more directly, we obtained longitudinal samples of venous blood from multiple sclerosis patients undergoing treatment with fingolimod (FTY-720), a drug that prevents sphingosine-1-phosphate (S1P)-mediated lymphocyte egress from LTs and NLTs (Figure 6D). The absolute numbers and frequencies of naive CD4$^+$ (Figures S4A and S4B) and CD8$^+$ T cells (Figures 6E, S4C, and S4D) fell within the first month and remained low with continuous treatment over a period of 6 months. A similar but less dramatic pattern was observed for memory CD4$^+$ (Figures S4A and S4B) and CD8$^+$ T cells (Figures 6E, S4C, and S4D). The residual memory CD4$^+$ T cell populations exhibited a predominant T$_{EM}$ phenotype (Figures S4A and S4B), and the residual CD8$^+$ T cell populations exhibited a predominant T$_{EMRA}$ phenotype (Figures 6E, S4C, and S4D). Moreover, approximately 80% of the residual memory CD8$^+$ T cells expressed GzmB and perforin after 6 months, and the absolute counts of memory CD8$^+$ T cells that expressed both GzmB and perforin were not significantly lower after 6 months (Figure 6F). These changes were reflected in the activation-induced functional profiles of memory CD8$^+$ T cells, which less commonly produced IL-2 and more commonly upregulated GzmB and perforin after 6 months compared with matched samples obtained before the initiation of FTY-720 (Figure 6G). In line with these findings, the absolute numbers of CCR7$^-$CD27$^-$CX3CR1$^+$ memory CD8$^+$ T cells remained stable over time, whereas the absolute numbers and frequencies of CCR7$^-$CD27$^+$CX3CR1$^-$ memory CD8$^+$ T cells declined over time, leading to a proportionate increase in the frequencies of CCR7$^-$CD27$^-$CX3CR1$^+$ memory CD8$^+$ T cells (Figure 6H). Various chemokine receptors and other homing molecules were also expressed less frequently among CCR7$^-$CD27$^-$CX3CR1$^+$ memory CD8$^+$ T cells versus CCR7$^-$CD27$^+$CX3CR1$^-$ memory CD8$^+$ T cells in healthy donor PBMCs (Figure 6I).

Collectively, these data suggested that cytolytic CD8$^+$ T cells were selectively retained in the intravascular circulation and rarely migrated through LTs or NLTs.

Cytolytic and non-cytolytic effector memory CD8$^+$ T cells are transcriptionally and epigenetically distinct in the intravascular circulation

In further experiments, we used RNA-seq to identify the intravascular gene expression signatures of effector memory CD8$^+$ T cells with a cytolytic phenotype (CCR7$^-$CD27$^-$CX3CR1$^+$) and effector memory CD8$^+$ T cells with a non-cytolytic phenotype (CCR7$^-$CD27$^+$CX3CR1$^-$), akin to those detected in TDL (Figure S5A). Core signatures of differentially expressed genes (fold change > 2; $p < 0.05$) were identified among the CCR7$^-$CD27$^+$CX3CR1$^-$ (633 genes) and CCR7$^-$CD27$^-$CX3CR1$^+$ subsets (545 genes), including transcripts encoding various costimulatory and effector molecules, integrins, trafficking receptors, and transcription factors (Figures S5A and S5B and Table S4). Gene ontology (GO) analysis revealed that CCR7$^-$CD27$^+$CX3CR1$^-$ cells were enriched for signatures associated with adhesion, migration, and proliferation, whereas CCR7$^-$CD27$^-$CX3CR1$^+$ cells were enriched for signatures associated with granule localization, epigenetic regulation, and lymphocyte differentiation (Figure S5C). The gene signature of CCR7$^-$CD27$^+$CX3CR1$^-$ cells also overlapped with the gene signature of memory precursors (IL-7R^{hi}) in the CD8$^+$ lineage, determined using GSEA (Figure S5D). Accordingly, expression levels of IL-7R and TCF-1 readily distinguished the CCR7$^-$CD27$^+$CX3CR1$^-$ and CCR7$^-$CD27$^-$CX3CR1$^+$ populations

(Figure S5E), and CCR7$^-$CD27$^+$CX3CR1$^-$ cells proliferated in vitro more vigorously than CCR7$^-$CD27$^-$CX3CR1$^+$ cells (Figure S5F). Many of the integrins and trafficking receptors were also differentially expressed at the protein level (Figures 6I and S5G).

To determine if these transcriptional differences were associated with distinct transcription factor motifs and OCRs, we used ATAC-seq to map the corresponding epigenetic landscapes. CCR7$^-$CD27$^+$CX3CR1$^-$ cells contained more OCRs (n = 4,426) than CCR7$^-$CD27$^-$CX3CR1$^+$ cells (n = 1,732) (Tables S5 and S6). Most of these OCRs were located in introns or intergenic regions (Figure S6A). Transcription factor motif analysis revealed that OCRs unique to the CCR7$^-$CD27$^+$CX3CR1$^-$ subset contained binding sites for the ATF family, whereas OCRs unique to the CCR7$^-$CD27$^-$CX3CR1$^+$ subset contained binding sites for the RUNX, BORIS, and TBOX families (Figure S6B). Specific regions next to genes associated with self-renewal (*Cd28*, *Il7r*, *Kit*, and *Tcf7*) and effector functions (*Gzmh*, *Gzmb*, *Prf1*, and *Cx3cr1*) were also differentially accessible between the CCR7$^-$CD27$^+$CX3CR1$^-$ and CCR7$^-$CD27$^-$CX3CR1$^+$ subsets (Figures S6C and S6D).

Collectively, these results indicated that intravascular CCR7$^-$CD27$^+$CX3CR1$^-$ memory CD8$^+$ T cells, like their non-cytolytic T$_{EM}$ and T$_{EMRA}$ counterparts in TDL, were transcriptionally and epigenetically distinct from intravascular CCR7$^-$CD27$^-$CX3CR1$^+$ memory CD8$^+$ T cells.

Virus-specific CD8$^+$ T cells rarely express cytolytic molecules in TDL

To confirm these findings in the context of antigen specificity, we obtained paired samples of blood and TDL from individuals with chronic HIV infection. In matched samples, CMV-specific CD8$^+$ T cells were proportionately more common in blood versus TDL (median ratio = 2.8), whereas HIV-specific CD8$^+$ T cells, which displayed a transitional memory phenotype (CCR7$^-$CD27$^+$CD45RO$^+$) in both compartments (Figure S7A) (Buggert et al., 2014), were proportionately less common in blood versus TDL (median ratio = 0.79) (Figure 7A). The expression of cytolytic molecules was confined almost exclusively to intravascular virus-specific CD8$^+$ T cells (Figure 7B). Accordingly, most CMV-specific CD8$^+$ T cells in blood displayed a CCR7$^-$CD27$^-$ phenotype and expressed GzmB, whereas most CMV-specific CD8$^+$ T cells in TDL displayed a CCR7$^-$CD27$^+$ phenotype and lacked GzmB (Figure 7C). Moreover, a direct correlation was observed between the frequency of intrasvascular virus-specific CD8$^+$ T cells that expressed both GzmB and perforin and the relative frequency of virus-specific CD8$^+$ T cells in blood versus TDL (Figure 7C). In line with these findings, relatively few Eomes^{lo}T-bet^{hi} virus-specific CD8^{+} T cells were present in TDL (Figure 7D).

To determine the clonal origins of these anatomically and functionally distinct virus-specific CD8^{+} T cell populations, we sequenced the corresponding *TRB* gene rearrangements in blood and TDL. As expected, the CMV-specific repertoires were heavily skewed in favor of a single clonotype, whereas the HIV-specific repertoires incorporated higher frequencies of subdominant clonotypes (Figures 7E and S7B). A very high degree of clonotypic overlap was also observed between matched specificities in blood and TDL (Figure S7C).

We then used a combined single-cell approach to compare the transcriptomes of clonotypically matched CMV-specific and HIV-specific CD8^{+} T cells in blood and TDL. Intravascular CMV-specific CD8^{+} T cell clonotypes more commonly expressed various effector genes, including *Gzmb*, *Gzmh*, *Gnly*, *Prf1*, *Ccl4*, *Fgfbp2*, *Cx3cr1*, and *Nkg7*, and less commonly expressed genes associated with early differentiation, including *Gzmk*, *Il7r*, *Tcf7*, *Cd27*, *Ccr7*, and *Nell2*, relative to their counterparts in TDL (Figure 7F). A similar pattern was observed among HIV-specific CD8^{+} T cell clonotypes, which displayed an effector-like gene expression profile in blood and a stem-like gene expression profile in TDL (Figure 7G).

Collectively, these findings demonstrated that functionally, phenotypically, and transcriptionally distinct virus-specific CD8^{+} T cells with shared clonal ancestries recirculated in blood and TDL.

DISCUSSION

Elegant work over several decades has enhanced our understanding of anatomically localized and intravascular subsets of memory $CD8^+$ T cells (Kumar et al., 2017; Sallusto et al., 1999; Sathaliyawala et al., 2013). In contrast, relatively little information has emerged about the nomadic $CD8^+$ T cell populations that recirculate continuously and survey peripheral tissue sites. In this body of work, we characterized the functional, phenotypic, and transcriptional properties of tissue-emigrant $CD8^+$ T cells in humans and rhesus macaques. Our key finding was that not all memory $CD8^+$ T cell subsets migrated through LTs or NLTs. Effector memory $CD8^+$ T cell subsets that expressed high levels of cytolytic molecules were rarely detected in tissues or TDL. Instead, these cells were selectively retained in the intravascular circulation, persisting for months after inhibition of S1P-dependent tissue egress by FTY-720. In addition, we identified previously unrecognized progenitor-like subsets of $CD8^+$ T cells within the classically defined T_{EM} and T_{EMRA} compartments that migrated through tissues and TDL.

Since the pioneering work of Gowans and colleagues (Gowans, 1957, 1959; Gowans and Knight, 1964), our understanding of human lymphocyte recirculation and tissue egress has been primarily shaped via studies in animal models (Hall and Morris, 1965; Mackay et al., 1996; Mackay et al., 1988; Mackay et al., 1990; Mackay et al., 1992; Miller and Sprent, 1971; Smith et al., 1970; Sprent, 1973). However, these studies lacked the technology to examine migratory lymphocyte populations in detail, and the reported findings cannot necessarily be extended to humans or non-human primates (Beura et al., 2016). Only a limited number of studies have been conducted on lymphocyte trafficking via efferent lymph in humans (Buggert et al., 2018; Fox et al., 1984; Girardet and Benninghoff, 1977; Klicznik et al., 2019; Lemaire et al., 1998; Vella et al., 2019; Voillet et al., 2018). In contrast to these efforts, we used state-of-the-art technology to map the entire immune system in TDL. A vast majority of immune cells in efferent lymph were T cells (75%). Other lineages commonly found in the intravascular circulation, such as monocytes, neutrophils, and myeloid-derived DCs, were rarely detected in clean samples of efferent lymph, concordant with their distinct origins and differentiation pathways (Furze and Rankin, 2008; Zhao et al., 2018), whereas NK cells were present at largely equivalent frequencies in blood and TDL (Fox et al., 1984).

In contrast to landmark ovine studies, which reported that >90% of all T cells in efferent lymph displayed a naive phenotype (Mackay et al., 1988; Mackay et al., 1990), we found that naive T cell frequencies ranged from <20% to >90% in human and non-human TDL. Classically defined CD8$^+$ T$_{EM}$ and T$_{EMRA}$ cells were also present in efferent lymph, but unlike the corresponding intravascular subsets, these cells were not highly differentiated and rarely expressed cytolytic molecules. Intralymphatic CD8$^+$ T$_{EM}$ and T$_{EMRA}$ cells instead exhibited progenitor-like characteristics, including the ability to proliferate in response to activation and produce IL-2. These cells were functionally and transcriptionally equivalent to intravascular T$_{CM}$ cells and lacked the tissue residency marker CD69. Accordingly, genes and pathways associated cell cycle transition, chemotaxis, self-renewal, telomere maintenance, and trafficking were upregulated among intralymphatic versus intravascular CD8$^+$ T$_{EM}$ and T$_{EMRA}$ cells, whereas genes and pathways associated with cytolytic activity and effector functionality were downregulated among intralymphatic versus intravascular CD8$^+$ T$_{EM}$ and T$_{EMRA}$ cells. Moreover, intralymphatic CD8$^+$ T$_{EM}$ and T$_{EMRA}$ cells exhibited a stem-like Eomes^{hi}T-bet^{lo}TCF-1^{hi} transcriptional profile (Im et al., 2016; Siddiqui et al., 2019), unlike intravascular CD8$^+$ T$_{EM}$ and T$_{EMRA}$ cells (McLane et al., 2013). Of note, murine studies have identified a migratory CCR7$^-$CX3CR1^{int} population in blood, efferent lymph, and tissues (Gerlach et al., 2016). A vast majority of human CCR7$^-$ memory CD8$^+$ T cells in efferent lymph and tissues nonetheless displayed a CD27$^+$CX3CR1$^-$ phenotype, conceivably indicating adaptations to recurrent pathogen exposure over a long period of time.

Memory CD8$^+$ T cells rarely expressed GzmB and perforin in TDL and almost never expressed GzmB and perforin in LTs and NLTs. A similar pattern was observed for persistent virus-specific CD8$^+$ T cells in TDL. These findings suggested that cytolytic CD8$^+$ T cells were largely confined to the intravascular circulation, both under physiological conditions and during chronic infection with CMV or HIV. Several observations further argued against the possibility that cytolytic molecules were transiently downregulated as memory CD8$^+$ T cells entered the peripheral tissues, a process that would require granule autophagy, extensive transcriptional changes, and epigenetic remodeling at effector gene loci, with reversal of these adaptations after transit and continual plasticity to maintain a state of phenotypic oscillation in response to microenvironmental signals. First, epigenetic analyses confirmed the presence of multiple OCRs adjacent to effector genes, such as *Gzmb*, *Gzmh*, *Prf1*, and *Tbx21*, among intravascular but not among intralymphatic CD8$^+$ T$_{EM}$ and T$_{EMRA}$ cells, suggesting a stable phenotype rather than a transitory state. Second, mixing experiments showed that neither efferent lymph nor plasma altered the expression of GzmB expression among CD8$^+$ T$_{EM}$ and T$_{EMRA}$ cells isolated from blood or TDL.

Third, cytolytic CCR7$^-$CX3CR1$^+$ memory CD8$^+$ T cells exhibited skewed clonotypic profiles compared with their non-cytolytic T$_{CM}$ (CCR7$^+$CX3CR1$^-$) and T$_{EM}$ counterparts (CCR7$^-$CX3CR1$^-$) in blood and TDL. Fourth, the absolute numbers of T$_{EM}$ and T$_{EMRA}$ cells remained stable in the intravascular circulation after inhibition of S1P-dependent tissue egress via the administration of FTY-720. Cytolytic subsets of memory CD8$^+$ T cells therefore appeared to be selectively retained in the intravascular space, consistent with the findings of a previous study (Gerlach et al., 2016).

The general absence of cytolytic CD8$^+$ T cells in tissues hinted at the existence of an evolutionarily conserved mechanism that might operate to minimize collateral tissue damage during normal homeostasis. In this scenario, cytolytic CD8$^+$ T cells would reside in the bloodstream under physiological conditions, acting as a reservoir that could be mobilized rapidly in response to infection, inflammation, or injury anywhere in the body, akin to neutrophils. Previous studies have shown that CD8$^+$ T cells loaded with perforin and serine proteases infiltrate tissue sites of pathology in many autoimmune diseases, cancers, and chronic infections (Boschetti et al., 2016; Duhen et al., 2018; Nguyen et al., 2019; Reuter et al., 2017; Strioga et al., 2011). However, most of these anatomically discrete cell populations were locally induced or constitutively resident, in contrast to non-resident cytolytic CD8$^+$ T cells (CD69$^-$CX3CR1$^+$) derived from the intravascular circulation (Buggert et al., 2018; Duhen et al., 2018). Many intracellular pathogens infect lymphocytes, other blood cells, or vascular endothelial cells (Friedman et al., 1981), as reviewed previously (Valbuena and Walker, 2006). Our data therefore suggested another possible scenario, namely a particular role for cytolytic immune surveillance in the intravascular compartment. In line with this concept, CMV-specific CD8$^+$ T cells often circulate at high frequencies in the vasculature (Gordon et al., 2017), likely as a consequence of viral persistence in endothelial cells (Jarvis and Nelson, 2007), and typically display a cytolytic phenotype characterized by high expression levels of GzmB, perforin, and CX3CR1 (Appay et al., 2000; Buggert et al., 2014). Fractalkine, the ligand for CX3CR1, is expressed on the membrane of activated vascular endothelial cells, where it plays a critical role in leukocyte recruitment (Schulz et al., 2007), rolling (Imai et al., 1997), and adhesion (Fong et al., 1998). These collective properties could facilitate effective CD8$^+$ T cell-mediated immune surveillance under the shear flow conditions that characterize the vascular environment. Of note, intravascular confinement does not necessarily preclude access to tissues. Cytolytic CD8$^+$ T cells are abundant in highly perfused organs, such as bone marrow and spleen (Buggert et al., 2018; Sathaliyawala et al., 2013). Moreover, several organs, including the kidneys and liver, contain fenestrated epithelia, which enable intravascular cytolytic CD8$^+$ T cells to arrest and engage target cells via cytoplasmic protrusions (Guidotti et al., 2015).

On the basis of our findings, we propose that circulating effector memory CD8$^+$ T cells can be divided into two distinct subsets, namely a constitutively intravascular CCR7$^-$CD27$^-$CX3CR1$^+$ subset with cytolytic properties and a tissue-trafficking CCR7$^-$CD27$^+$CX3CR1$^-$ subset with stem-like properties. Importantly, we found that CD27$^-$ T$_{EM}$ and T$_{EMRA}$ cells were clonotypically, epigenetically, functionally, and transcriptionally distinct from CD27$^+$ T$_{EM}$ and T$_{EMRA}$ cells, which resembled T$_{CM}$ cells in blood and TDL. Accordingly, the intravascular CCR7$^-$CD27$^+$CX3CR1$^-$ subset likely contained the migratory CCR7$^-$CD27$^+$CX3CR1$^-$ subset identified in TDL. Tissue-emigrant CD8$^+$ T cells in the intravascular T$_{EM}$/T$_{EMRA}$ compartment might therefore be defined by the expression of CD27.

Intravascular HIV-specific CD8$^+$ T cells in individuals with chronic progressive disease typically express a transitional memory phenotype (CCR7$^-$CD27$^+$CD45RA$^-$), which has generally been associated with functional exhaustion and defective maturation (Buggert et al., 2014; Champagne et al., 2001). In the context of our data, this phenotype might instead define tissue-trafficking cells, which could potentially access virally infected targets in LTs and NLTs (Buggert et al., 2018; Nguyen et al., 2019; Reuter et al., 2017). We also found that functionally and phenotypically distinct virus-specific CD8$^+$ T cells were clonotypically related but transcriptionally divergent in blood and TDL. This particular observation suggested that individual precursors in the naive CD8$^+$ T cell pool differentiated into antigen-experienced memory subsets with distinct migratory properties, consistent with previous descriptions of multiple fates at the functional level (Gerlach et al., 2013; Gerlach et al., 2010).

In summary, we have provided a comprehensive atlas of the recirculating immune system in humans and identified a core signature that defines tissue-emigrant CD8$^+$ T cells under homeostatic conditions. Our collective dataset might feasibly inform new developments in the field of immunotherapy, which is currently limited by several parameters, including the longevity of cell infusates and access to sites of pathology. In this light, the characterization of intravascular effector memory CD8$^+$ T cells with stem-like properties and unrestricted trafficking pathways through peripheral tissues could rationalize attempts to engineer more effective cellular therapies, especially in the context of solid tumors and persistent viruses that establish latent infections, such as HIV.

STAR METHODS

KEY RESOURCES TABLE

REAGENT or RESOURCE	SOURCE	IDENTIFIER
Antibodies		
3A9 (BV650) [anti-CCR5]	BD Biosciences	564999 (RRID:AB_2739037)
UCHT1 (AF700) [anti-CD3]	BD Biosciences	561027 (RRID:AB_10561682)
UCHT1 (APC-R700) [anti-CD3]	BD Biosciences	565119 (RRID:AB_2744385)
M-A251 (PE) [anti-CD25]	BD Biosciences	555432 (RRID:AB_395826)
HI100 (BV650) [anti-CD45RA]	BD Biosciences	563963 (RRID:AB_2738514)
HI100 (PE-CF594) [anti-CD45RA]	BD Biosciences	562298 (RRID:AB_11154413)
UCHL1 (BV650) [anti-CD45RO]	BD Biosciences	563749 (RRID:AB_2744412)
UCHL1 (PE-CF594) [anti-CD45RO]	BD Biosciences	562299 (RRID:AB_11154398)
C3 II.1 (BV421) [anti-CD49c]	BD Biosciences	744516 (RRID:AB_2742290)
DX2 (BB515) [anti-CD95]	BD Biosciences	564596 (RRID:AB_2744470)
RF8B2 (AF488) [anti-CXCR5]	BD Biosciences	558112 (RRID:AB_397034)
RF8B2 (AF647) [anti-CXCR5]	BD Biosciences	558113 (RRID:AB_2737606)
GB11 (Alexa700) [anti-GzmB]	BD Biosciences	560213 (RRID:AB_1645453)
G46-6 (BV605) [anti-HLA-DR]	BD Biosciences	562844 (RRID:AB_2744478)
G46-6 (BV650) [anti-HLA-DR]	BD Biosciences	564231 (RRID:AB_2738685)
B56 (FITC) [anti-Ki67]	BD Biosciences	556026 (RRID:AB_396302)
ACT35 (APC) [anti-OX40]	BD Biosciences	563473 (RRID:AB_2738230)
MAb11 (PE-Cy7) [anti-TNF]	BD Biosciences	560678 (RRID:AB_1727578)
SP34-2 (APC-Cy7) [anti-CD3]	BD Biosciences	557757 (RRID:AB_396863)
DX2 (PE-Cy5) [anti-CD95]	BD Biosciences	559773 (RRID:AB_397317)
GB11 (AF700) [anti-GzmB]	BD Biosciences	560213 (RRID:AB_1645453)
L293/L25 [anti-CD28/CD49d]	BD Biosciences	347690 (RRID:AB_647457)
C92-605 (FITC) [anti-active caspase-3]	BD Biosciences	559341 (RRID:AB_397234)
SK7 (PE) [anti-CD3]	BD Biosciences	560761 (RRID:AB_1727478)
CD28.2 (ECD) [anti-CD28]	Beckman Coulter	6607111 (RRID:AB_1575955)
4B4-1 (BV421) [anti-4-1BB]	BioLegend	309819 (RRID:AB_10895902)
G043H7 (APC-Cy7) [anti-CCR7]	BioLegend	353211 (RRID:AB_10915272)
UCHT1 (BV711) [anti-CD3]	BioLegend	300463 (RRID:AB_2566035)
RPA-T8 (BV570) [anti-CD8a]	BioLegend	301038 (RRID:AB_2563213)
RPA-T8 (BV605) [anti-CD8a]	BioLegend	301039 (RRID:AB_11126985)
RPA-T8 (BV711) [anti-CD8a]	BioLegend	301043 (RRID:AB_11218793)
RPA-T8 (BV785) [anti-CD8a]	BioLegend	301045 (RRID:AB_11219195)
ICRF44 (PE-Cy5) [anti-CD11b]	BioLegend	301307 (RRID:AB_314159)
M5E2 (BV510) [anti-CD14]	BioLegend	301842 (RRID:AB_2561946)
1B4 (PE-Cy7) [anti-CD18]	BioLegend	373409 (RRID:AB_2716025)
HIB19 (BV510) [anti-CD19]	BioLegend	302242 (RRID:AB_2561668)
O323 (AF700) [anti-CD27]	BioLegend	302813 (RRID:AB_493756)
O323 (BV650) [anti-CD27]	BioLegend	302827 (RRID:AB_11124941)
O323 (BV785) [anti-CD27]	BioLegend	302831 (RRID:AB_11219185)
TS2/16 (AF700) [anti-CD29]	BioLegend	303019 (RRID:AB_2130079)
HIT2 (APC) [anti-CD38]	BioLegend	303510 (RRID:AB_314362)
HIT2 (BV711) [anti-CD38]	BioLegend	303527 (RRID:AB_11218990)
TS2/7 (PE-Cy7) [anti-CD49a]	BioLegend	328311 (RRID:AB_2566271)
P1E6-C5 (APC) [anti-CD49b]	BioLegend	359309 (RRID:AB_2564198)

GoH3 (BV650) [anti-CD49f]	BioLegend	313629 (RRID:AB_2686989)
HI186 (FITC) [anti-CD52]	BioLegend	316003 (RRID:AB_389276)
FN50 (BV421) [anti-CD69]	BioLegend	310929 (RRID:AB_10933255)
FN50 (PE-Cy5) [anti-CD69]	BioLegend	310907 (RRID:AB_314842)
Ber-ACT8 (BV605) [anti-CD103]	BioLegend	350217 (RRID:AB_2564282)
Ber-ACT8 (PE-Cy7) [anti-CD103]	BioLegend	350211 (RRID:AB_2561598)
2A9-1 (PE) [anti-CX3CR1]	BioLegend	341604 (RRID:AB_1595456)
2A9-1 (APC) [anti-CX3CR1]	BioLegend	34161 (RRID:AB_2087424)
5E8 (FITC) [anti-CXCR2]	BioLegend	310720 (RRID:AB_2571959)
G025H7 (BV711) [anti-CXCR3]	BioLegend	353731 (RRID:AB_2563532)
K041E5 (BV421) [anti-CXCR6]	BioLegend	356013 (RRID:AB_2562514)
EH12.2H7 (BV421) [anti-PD-1]	BioLegend	329919 (RRID:AB_10900818)
EH12.2H7 (PE) [anti-PD-1]	BioLegend	329906 (RRID:AB_940483)
10F.9G2 (BV785) [anti-PD-L1]	BioLegend	124331 (RRID:AB_2629659)
B-D48 (BV421) [anti-perforin]	BioLegend	353307 (RRID:AB_11149688)
B-D48 (PE-Cy7) [anti-perforin]	BioLegend	353315 (RRID:AB_2571972)
4B10 (PE-Dazzle 594) [anti-T-bet]	BioLegend	644827 (RRID:AB_2565676)
RPA-T8 (BV570) [anti-CD8a]	BioLegend	301038 (RRID:AB_2563213)
M5E2 (BV650) [anti-CD14]	BioLegend	301835 (RRID:AB_11204241)
3G8 (BV650) [anti-CD16]	BioLegend	302042 (RRID:AB_2563801)
2H7 (BV650) [anti-CD20]	BioLegend	302335 (RRID:AB_11218609)
UCTH1 [anti-CD3]	Bio-Rad	MCA463GT (RRID:AB_1101798)
C63D9 (PE) [anti-TCF-1]	Cell Signaling Technology	14456 (RRID:AB_2798483)
WD1928 (AF647) [anti-Eomes]	eBioscience	50-4877-42 (RRID:AB_2574229)
ISA-3 (PE-EF610) [anti-ICOS]	eBioscience	61-9948-41 (RRID:AB_2574683)
dG9 (PE-Cy7) [anti-perforin]	eBioscience	25-9994-42 (RRID:AB_2573574)
4B10 (PE) [anti-T-bet]	eBioscience	12-5825-82 (RRID:AB_925761)
4B10 (PE-Cy7) [anti-T-bet]	eBioscience	25-5825-82 (RRID:AB_11042699)
pf344 (FITC) [anti-perforin]	Mabtech AB	3465-7 (RRID:AB_1925742)
Act-1 (FITC) [anti-α4β7]	NIH AIDS Reagent Program	BE0034 (RRID:AB_1107713)
S3.5 (PE-Cy5.5) [anti-CD4]	Thermo Fisher Scientific	MHCD0418 (RRID:AB_10376013)
B27 (AF700) [anti-IFNγ]	Thermo Fisher Scientific	506515 (RRID:AB_961353)
S3.5 (PE-Cy5.5) [anti-CD4]	Thermo Fisher Scientific	MHCD0418 (RRID:AB_10376013)
Biological Samples		
Peripheral blood and TDL from HIV$^-$ individuals undergoing thoracic duct cannulation for idiopathic or traumatic chylopericardium, chylothorax, and/or chylous ascites	University of Pennsylvania or Children's Hospital of Philadelphia	N/A
Matched arterial and venous blood samples from HIV$^-$ individuals undergoing thoracic duct cannulation for idiopathic or traumatic chylopericardium, chylothorax, and/or chylous ascites	University of Pennsylvania	N/A

Non-enlarged tonsils from patients undergoing tonsillectomy for sleep apnea	University of Pennsylvania	N/A
Macroscopically normal mesenteric LNs from patients undergoing abdominal surgery for various indications	Case Western Reserve University	N/A
Macroscopically normal iliac LNs from kidney transplant donors	University of Pennsylvania	N/A
Liver biopsies from liver transplant donors	Karolinska University Hospital	N/A
Decidua isolated from the first trimester	Karolinska University Hospital	N/A
Colon sections from patients undergoing abdominal surgery for various indications	University of Pennsylvania	N/A
Venous blood from multiple sclerosis patients before and during FTY-720 treatment	McGill University	N/A
Matched central and portal blood samples from liver transplant donors	Hanover Hospital	N/A
Peripheral blood, tissues, and TDL from rhesus macaques	Oregon National Primate Research Center or Children's Hospital of Pennsylvania	N/A
Chemicals, Peptides, and Recombinant Proteins		
LIVE/DEAD Fixable Aqua	Thermo Fisher Scientific	Cat#L34957
LIVE/DEAD Fixable Violet	Thermo Fisher Scientific	Cat#L34955
TFL4	OncoImmun	N/A
CTV	Thermo Fisher Scientific	Cat#C34557
Ethiodol	Savage Laboratories	N/A
PMA	Sigma-Aldrich	Cat#P1585
Ionomycin	Sigma-Aldrich	Cat#I3909
Lysis buffer	Takara	Cat#635013
Tn5 transposase	Illumina	Cat#20034197
RNAzol	Molecular Research Center	Cat#DN-127
Critical Commercial Assays		
Cytofix/Cytoperm Buffer Kit	BD Biosciences	Cat#554714
FoxP3 Transcription Factor Buffer Kit	eBioscience	Cat#00-5521-00
SMART-Seq v4 Ultra Low Input RNA Kit	Takara	Cat#634888
Nextera XT DNA Library Prep Kit	Illumina	Cat#FC-131-1024
CD8$^+$ T Cell Enrichment Kit	StemCell Technologies	Cat#19159
MinElute Reaction Cleanup Kit	Qiagen	Cat#28204
QIAQuick PCR Purification Kit	Qiagen	Cat#28104
Chromium Next GEM Single Cell 5' Library & Gel Bead Kit v1.1, 16 rxns	10X Genomics	Cat#1000165
Tube, Dynabeads MyOne SILANE - 2000048	10X Genomics	Cat#2000048
Chromium Next GEM Single Cell 5' Gel Bead Kit v1.1, 16 rxns - 1000169	10X Genomics	Cat#1000169
Chromium Next GEM Single Cell 5' Library Kit v1.1, 16 rxns - 1000166	10X Genomics	Cat#1000166
Chromium Next GEM Chip G Single Cell Kit, 48 rxns	10X Genomics	Cat#1000120
Chromium Single Cell 5' Library Construction Kit, 16 rxns	10X Genomics	Cat# 1000020

Single Index Kit T Set A, 96 rxns	10X Genomics	Cat# 1000213
Deposited Data		
ATAC-seq data processing pipeline	GitHub	https://github.com/wherrylab/jogiles_ATAC/blob/master/Giles_Wherry_ATAC_pipeline_hg19_UPennCluster.sh
Sequence datasets in Gene Expression Omnibus	NCBI	https://www.ncbi.nlm.nih.gov/geo/summary/
Software and Algorithms		
FlowJo version 9.8.8 or higher	Tree Star	https://www.flowjo.com/
FlowJo version 10.6.1	Tree Star	https://www.flowjo.com/
STAR software version 2.5.2a	STAR	N/A
DESeq2	Bioconductor	https://bioconductor.org/packages/release/bioc/html/DESeq2.html
R limma package version 3.28	Bioconductor	https://bioconductor.org/packages/release/bioc/html/limma.html
Ingenuity Pathway Analysis	Qiagen Bioinformatics	N/A
Pheatmap version 1.0.12 package in R	RStudio	N/A
Ggplot version 3.1.0 package in Prism	RStudio	N/A
RStudio	RStudio	https://rstudio.com
Prism version 7.0	GraphPad Software Inc.	https://www.graphpad.com/
Software for GSEA analysis	Broad Institute	http://www.broadinstitute.org/gsea/index.jsp
Broad Institute Database	Broad Institute	https://www.broadinstitute.org/data-software-and-tools
Bowtie2 (Fastq files aligment to hg19)	Johns Hopkins University	http://www.bowtie-bio.sourceforge.net/bowtie2
SAMtools (in ATAC-seq, to remove mitochondrial reads)	GitHub	http://www.htslib.org
Picard (in ATAC-seq, to remove duplicates)	GitHub	https://broadinstitute.github.io/picard
Bedtools subtract (in ATAC-seq, to remove blacklist regions)	Bedtools	https://bedtools.readthedocs.io
MACS2	GitHub	https://pypi.python.org/pypi/MACS2
HOMER (in ATAC-seq)	HOMER	http://homer.ucsd.edu/homer
Integrative Genomics Viewer software version 2.5.2 (in ATAC-seq)	Broad Institute	https://software.broadinstitute.org/software/igv
Custom Java script and BLAST	National Center for Biotechnology Information	https://blast.ncbi.nlm.nih.gov/Blast.cgi
SPICE version 6.0		https://niaid.github.io/spice
Cell Ranger version 4.0.0	10X Genomics	https://support.10xgenomics.com/single-cell-gene-expression/software/pipelines/latest/installation
Cell Ranger mkfastq with bcl2fastq2 version 2.20.0.422	10X Genomics	N/A
Seurat version 3.2	RStudio	https://github.com/satijalab/seurat/archive/v3.2.1.zip
SCTransform	RStudio	N/A
Vision 2.1	N/A	N/A
Other		
FACSAriaII	BD Biosciences	N/A
NextSeq 550	Illumina	N/A

HiSeq 4000	Illumina	N/A
NovaSeq 6000	Illumina	N/A
Qubit 4 Fluorometer	Thermo Fisher Scientific	N/A

RESOURCE AVAILABILITY

Lead contact

Further information and requests for reagents and resources should be directed to and will be fulfilled by the Lead Contact, Michael R Betts, University of Pennsylvania, (betts@pennmedicine.upenn.edu).

Materials availability

MHC class I tetramers can be generated and shared on a collaborative basis.

Data and code availability

The sequence datasets reported in this paper have been deposited in the Gene Expression Omnibus under accession no. XXX.

EXPERIMENTAL MODEL AND SUBJECT DETAILS

Human samples

Matched peripheral blood and TDL samples were collected from HIV$^-$ individuals undergoing thoracic duct cannulation for idiopathic or traumatic chylopericardium, chylothorax, and/or chylous ascites (n = 52; University of Pennsylvania or Children's Hospital of Philadelphia). Matched arterial and venous blood samples were obtained from some of these patients (n = 3; University of Pennsylvania). Additional samples were collected from HIV$^+$ donors with no clinical indication for thoracic duct cannulation via a research protocol (n = 10; University of Pennsylvania). Donor groups and clinical parameters are summarized in Table S1. Lymphoid and non-lymphoid organs or tissues were obtained as follows: non-enlarged tonsils from patients undergoing tonsillectomy for sleep apnea (n = 7; University of Pennsylvania), macroscopically normal mesenteric LNs from patients undergoing abdominal surgery for various indications (n = 8; Case Western Reserve University), macroscopically normal iliac LNs from kidney transplant donors (n = 6; University of Pennsylvania), liver biopsies from liver transplant donors (n = 6; Karolinska University Hospital), decidua from first-trimester pregnancies (n = 3; Karolinska

University Hospital), and colon sections from patients undergoing abdominal surgery for various indications (n = 3; University of Pennsylvania). Venous blood samples were collected from multiple sclerosis patients before and during treatment with FTY-720 (n = 12; McGill University). Matched central and portal blood samples were obtained from liver transplant donors (n = 3; Hanover Hospital). All participants enrolled in this study provided written informed consent in accordance with protocols approved by the regional ethical research boards and the Declaration of Helsinki.

Non-human primate samples

Rhesus macaque samples were obtained from the Oregon National Primate Research Center or the Children's Hospital of Pennsylvania. TDL was obtained via cannulation under anesthesia, and tissues were harvested at necropsy as described previously (Buggert et al., 2018). All procedures were conducted in accordance with federal statutes and regulations, including the Animal Welfare Act.

METHOD DETAILS

Cells and tissues

PBMCs were purified from whole blood or leukapheresis products via standard density gradient centrifugation and cryopreserved at −140°C. Lymph node mononuclear cells were isolated via mechanical disruption and cryopreserved at −140°C. Non-lymphoid mononuclear cells were isolated using a combination of mechanical disruption and collagenase treatment. TDL was accessed as described previously (Nadolski and Itkin, 2012). Briefly, a 25-gauge spinal needle was inserted under ultrasound guidance into an inguinal LN on each side of the body, and the oil-based contrast agent ethiodol (Savage Laboratories) was injected under fluoroscopic guidance into each LN. After opacification of the cisterna chyli, access was gained via an anterior transabdominal approach using a 21-gauge or a 22-gauge Chiba needle (Cook Medical Inc.), and a V-18 control guidewire (Boston Scientific) was inserted into the thoracic duct and manipulated cephalad, followed by a 60-cm 2.3F Rapid Transit Microcatheter (Cordis Corp.), which was advanced further into the thoracic duct to aspirate TDL. Aspirated TDL was collected in heparin tubes, and the contrast agent was removed via standard density gradient centrifugation. TDL samples were used directly in flow cytometry experiments or cryopreserved at −140°C.

Flow cytometry

Cells were stained as described previously (Buggert et al., 2018). Briefly, human cryopreserved mononuclear cells were thawed and rested for at least 1 hr in complete medium (RPMI-1640 supplemented with 10% fetal bovine serum, 1% L-glutamine, and 1% penicillin/streptomycin) in the presence of 10 U/mL DNAse I (Roche). Cells were then washed in phosphate-buffered saline (PBS), prestained for chemokine receptors and adhesion molecules for 10 min at 37°C, labeled with LIVE/DEAD Fixable Aqua (Thermo Fisher Scientific) for 10 min at room temperature, and stained with an optimized panel of directly conjugated monoclonal antibodies for a further 20 min at room temperature to detect additional surface markers. In some experiments, MHC class I tetramers were added for 10 min at room temperature immediately after washing in PBS. Cells were then washed in fluorescence-activated cell sorting (FACS) buffer (PBS containing 0.1% sodium azide and 1% bovine serum albumin) and fixed/permeabilized using a Cytofix/Cytoperm Buffer Kit (BD Biosciences) or a FoxP3 Transcription Factor Buffer Kit (eBioscience). Intracellular markers were detected via the subsequent addition of an optimized panel of directly conjugated antibodies for 1 hr at 37°C. Stained cells were fixed in PBS containing 1% paraformaldehyde (Sigma-Aldrich) and stored at 4°C. Similar procedures were used to characterize activated cells stimulated for 5 hr with PMA (5 ng/mL; Sigma-Aldrich) and ionomycin (500 ng/mL; Sigma-Aldrich) and proliferating cells stimulated for 5 days with α-CD3 (1 μg/mL; clone UCHT1; Bio-Rad) and α-CD28/CD49d (each at 1 μg/mL; clones L293/L25; BD Biosciences). Non-human primate cells were stained as described previously (Roberts et al., 2016). All samples were acquired within 3 days using an LSRII, an LSR Fortessa, or an LSR Symphony (BD Biosciences). Data were analyzed with FlowJo software version 9.8.8 or higher (Tree Star). The gating strategies are depicted in the relevant figures. All sorting experiments were performed using a FACSAriaII (BD Biosciences). Flow cytometry reagents are detailed in the Key Resources Table.

Tetramers

MHC class I tetramers conjugated to BV421 or PE were used to detect CD8$^+$ T cells with the following specificities: CMV NLVPMVATV (NV9/HLA-A*0201), HIV FLGKIWPSHK (FK10/HLA-A*0201), HIV ILKEPVHGV (IV9/HLA-A*0201), HIV SLYNTVATL (SL9/HLA-A*0201), HIV KYKLKHIVW (KW9/HLA-A*2402), HIV RYPLTFGW (RW8/HLA-A*2402), HIV GPGHKARVL (GL9/HLA-B*0702), HIV HPRVSSEVHI (HI10/HLA-B*0702), HIV SPAIFQSSF (SM9/HLA-B*0702), HIV

KRWIILGLNK (KK10/HLA-B*2705), HIV ISPRTLNAW (IW9/B*5701), HIV KAFSPEVIPMF (KF11/HLA-B*5701), and HIV QASQEVKNW (QW9/HLA-B*5701), and HIV TSTLQEQIGW (TW10/HLA-B*5701). All tetramers were generated in house as described previously (Price et al., 2005).

RNA-seq

RNA-seq was conducted as described previously (Buggert et al., 2018; Vella et al., 2019). Briefly, naive and memory CD8$^+$ T cells from mesenteric LNs, blood, and TDL (250 cells per subset) were sorted directly into lysis buffer (Takara) using a FACSAriaII (BD Biosciences) and frozen at −140°C. Libraries were prepared using the SMART-Seq v4 Ultra Low Input RNA Kit (Takara). PCR products were then indexed using a Nextera XT DNA Library Prep Kit (Illumina) and sequenced across 75 base pairs (bp) using a paired-end strategy with a 150-cycle high-output flow cell on a NextSeq 550 (Illumina). Three biological replicates were sequenced per experiment. Fastq files from replicate sequencing runs were concatenated and aligned to hg38 using STAR software version 2.5.2a. Mapped read depth ranged from 8 million to 75 million reads per sample. Aligned files were normalized using DESeq2 (Bioconductor).

Differentially expressed genes were identified among normalized RNA-seq counts from distinct subsets of CD8$^+$ T cells using a t-test ($p < 0.05$) in the R limma package (version 3.28). Genes of interest were then subjected to Ingenuity Pathway Analysis (Qiagen Bioinformatics). Heatmaps, PCA plots, and tSNE plots were created using the Pheatmap (version 1.0.12) and ggplot2 (version 3.1.0) packages in R or Prism version 7.0 (GraphPad). Normalized counts were also subjected to GSEA using software from the Broad Institute (http://www.broadinstitute.org/gsea/index.jsp). Gene signatures were compared with immunological and GO signatures from the Broad Institute Database.

Single-cell RNA-seq

Cryopreserved PBMCs and TDLMCs were thawed and rested overnight in complete medium at 37°C. Cells were then stained as described above, resuspended in RPMI medium without phenol red, and sorted directly into PBS supplemented with 10% FBS using a FACSAriaII (BD Biosciences). Each sorted bulk memory CD8$^+$ T cell population (n = 8,000 cells per sample) and each sorted tetramer$^+$ memory CD8$^+$ T cell population (n = 134–8,000 cells per sample) was loaded into a Chromium

Controller (10x Genomics). Sorted populations with fewer than 3,500 cells were combined with B cells from the same sample to enhance recovery (total n = 8,000 cells). Libraries for scRNA-seq and single-cell TCR-seq (scTCR-seq) were prepared according to the manufacturer's recommended protocols (10x Genomics). Samples were pooled and quantified using a TapeStation 2200 System (Agilent) with a Qubit 4 Fluorometer (Thermo Fisher Scientific). scRNAseq libraries were sequenced using a paired-end strategy with a 150-cycle high-output flow cell on a NovaSeq 6000 (Illumina), and scTCRseq libraries were sequenced using a paired-end strategy with a 150-cycle high-output flow cell on a NextSeq 550 (Illumina).

Data were processed initially using Cell Ranger version 4.0.0 (10X Genomics). Raw BCL files were demultiplexed and converted to fastq files using Cell Ranger mkfastq with bcl2fastq2 version 2.20.0.422 (10X Genomics). Cell Ranger count was used to align scRNA-seq reads to a GRCh38 reference to generate a count matrix for each sample, and Cell Ranger vdj was used to align scTCR-seq reads to a GRCh38 reference (10X Genomics). Data were analyzed using Seurat version 3.2. Cells with ≤200 or ≥3,000 transcripts and cells with ≥7% of reads mapping to mitochondrial genes were removed from the dataset. For antigen-specific analyses, cells with counts to genes containing the pattern IGH* and IGL* were excluded to remove B cells. Raw counts were merged across samples and normalized for integration using SCTransform (vars.to.regress = percent.mt, patient, and chip). Variable features were identified by SCTransform for PCA and UMAP calculations. Clusters were identified using the FindNeighbors and FindClusters (resolution = 0.5) functions. RNA count matrices were normalized prior to significance testing and visualization. Data visualization was performed using standard functions provided in ggplot2 and Seurat version 3.2. TCR clonotype metadata was added to the Seurat objects for clonotype analysis. Enrichment of previously reported memory T cell subset signatures (Cano-Gamez et al., 2020) in our dataset was determined using Vision 2.1 (DeTomaso and Yosef, 2016). The enrichment statistic was used to rename clusters as shown in Figure 3. The name of each cluster was the name of the gene signature with the highest enrichment statistic. For clusters with multiple similar enrichment statistics, the cluster was named using all enriched signatures, with the first name being the most highly enriched signature. For signatures that were enriched in multiple clusters, numbers were used to indicate strength of enrichment, with the strongest denoted as 1. GSEA was performed using the fgsea and msigdbr packages in R. Differential expression analysis was carried out using the FindMarkers function in

Seurat version 3.2. Genes were ranked in descending order based on the avg logFC before importing into fgsea (minSize = 10; maxSize = 500; nperm = 70,000).

Redirected killing assay

P815 mastocytoma target cells were labeled with LIVE/DEAD Fixable Violet (Thermo Fisher Scientific) and TFL4 (OncoImmun), washed twice in PBS, and incubated for 30 min at room temperature with α-CD3 (1 μg/mL; clone UCHT1; Bio-Rad). CD8$^+$ T cells were negatively selected from blood and TDL using a CD8$^+$ T Cell Enrichment Kit (StemCell Technologies). Isolated CD8$^+$ T cells were rested in complete medium for at least 45 min at 37°C and then incubated with α-CD3-coated P815 cells at different E:T ratios in a 96-well V-bottom plate for 4 hr at 37°C. Cells were then stained with α-active caspase-3–FITC (clone C92-605; BD Biosciences) and α-CD3–PE (clone SK7; BD Biosciences) and acquired using an LSRII (BD Biosciences). Cytolytic activity was calculated by subtracting the frequency of active caspase-3$^+$TFL4$^+$LIVE/DEAD$^-$ P815 cells in target-only wells from the frequency of active caspase-3$^+$TFL4$^+$LIVE/DEAD$^-$ P815 cells in wells containing CD8$^+$ T cells.

ATAC-seq

ATAC-seq was performed as described previously (Buenrostro et al., 2013) with minor modifications (Buggert et al., 2018). Briefly, memory CD8$^+$ T cells from blood, mesenteric LNs, and TDL (30,000–60,000 cells per subset) were sorted directly into complete medium using a FACSAriaII (BD Biosciences). Cells were then pelleted, washed with PBS, and treated with lysis buffer (10 mM Tris-HCl pH 7.4, 10 mM NaCl, 3 mM $MgCl_2$, 0.1% IGEPAL CA-630). Nuclear pellets were resuspended in the presence of Tn5 transposase (Illumina) for 30 min at 37°C. Tagmented DNA was purified using a MinElute Reaction Cleanup Kit (Qiagen). Amplified libraries were purified using a QIAQuick PCR Purification Kit (Qiagen) and sequenced across 75 or 100 bp using a paired-end strategy on a NextSeq 550 or a HiSeq4000 (Illumina). One or two biological replicates were sequenced per experiment.

The data processing pipeline is available at GitHub (https://github.com/wherrylab/jogiles_ATAC/blob/master/Giles_Wherry_ATAC_pipeline_hg19_UPennCluster.sh). Fastq files were aligned to hg19 using Bowtie2 (http://www.bowtie-bio.sourceforge.net/bowtie2). Unmapped, unpaired, and mitochondrial reads were removed using SAMtools (http://www.htslib.org). Duplicates were removed using Picard (https://broadinstitute.github.io/picard), and blacklist regions were removed using Bedtools subtract (https://bedtools.readthedocs.io). ATAC-seq peaks were called at a false discovery rate of 0.01 using MACS2 (https://pypi.python.org/pypi/MACS2). Normalization and differential peak analyses were performed using DESeq2 (Bioconductor) as described previously (Vella et al., 2019). Motif analyses were carried out using HOMER (http://homer.ucsd.edu/homer). ATAC-seq tracks were visualized using Integrative Genomics Viewer software version 2.5.2 (https://software.broadinstitute.org/software/igv).

TCR-seq

Expressed *TRB* gene rearrangements were sequenced as described previously (Boritz et al., 2016). Briefly, bulk memory or virus-specific CD8$^+$ T cells were sorted into cold fetal bovine serum and frozen in RNAzol (Molecular Research Center). TCRβ transcripts were amplified using a template-switch anchored RT-PCR. Libraries were sequenced across 150 bp using a paired-end strategy on a NextSeq 550 (Illumina). TCRβ sequences were annotated using a custom Java script and BLAST (National Center for Biotechnology Information). CDR3β sequences were assigned between the conserved cysteine at the 3' end of each *TRBV* gene and the conserved phenylalanine at the 5' end of each *TRBJ* gene. Unique TCRβ combinations were collapsed to determine clonotype counts.

QUANTIFICATION AND STATISTICAL ANALYSIS

Differences between unmatched groups were compared using an unpaired t-test or the Mann-Whitney *U* test, and differences between matched groups were compared using a paired t-test or the Wilcoxon signed-rank test. Non-parametric tests were used if the data were not distributed normally according to the Shapiro-Wilk test. Correlations were assessed using the Spearman rank correlation. All analyses were performed using RStudio (https://rstudio.com) or Prism version 7.0 (GraphPad). Functional profiles were compared using the permutation test in SPICE version 6.0 (https://niaid.github.io/spice). Phenotypic relationships within multivariate datasets were visualized using FlowJo software version 10.6.1 (Tree Star).

ACKNOWLEDGEMENTS

We express our gratitude to all study participants and funding agencies.

FUNDING

M.B. was supported by the Swedish Research Council, the Karolinska Institutet, the Swedish Society for Medical Research, the Jeansson Stiftelse, the Åke Wibergs Stiftelse, the Swedish Society of Medicine, the Cancerfonden, the Barncancerfonden, the Magnus Bergvalls Stiftelse, the Lars Hiertas Stiftelse, the Swedish Physician against AIDS Foundation, the Jonas Söderquist Stiftelse, and the Clas Groschinskys Minnesfond. Additional support was provided by R01 and R56 grants from the National Institutes of Health (AI076066, AI118694, and AI106481 to M.R.B.) and the Penn Center for AIDS Research (AI045008). D.A.P. was supported by a Welcome Trust Senior Investigator Award (100326/Z/12/Z).

AUTHOR CONTRIBUTIONS

M.B. and M.R.B. conceived the project; M.B. L.A.V., S.N., Z.C., T.S., A.P.P., C.M., A.R., L.K.C., A.S.J., I.B.B., M.I., and L.H. designed and performed experiments; M.B. L.A.V., S.N., V.W., T.S., A.P.P., S.M., S.D., J.B.G., O.R.B., J.P.A., M.E.J., and G.V. analyzed data; M.B., A.O., L.P., E.S., S.L.L., E.G., J.S., N.B., A.B.O., Y.D., A.N., D.H.C., D.A.P., I.F., D.C.D., E.J.W., M.G.I., and M.R.B. provided critical resources; M.B., N.B., D.H.C., T.M.L., A.D.W., D.A.P., D.C.D., E.J.W., and M.R.B. supervised experiments; M.B. and M.R.B. drafted the manuscript; M.B., D.A.P., and M.R.B. edited the manuscript.

COMPETING INTERESTS

The authors declare that they have no competing financial interests, patents, patent applications, or material transfer agreements associated with this study.

FIGURE LEGENDS

Figure 1

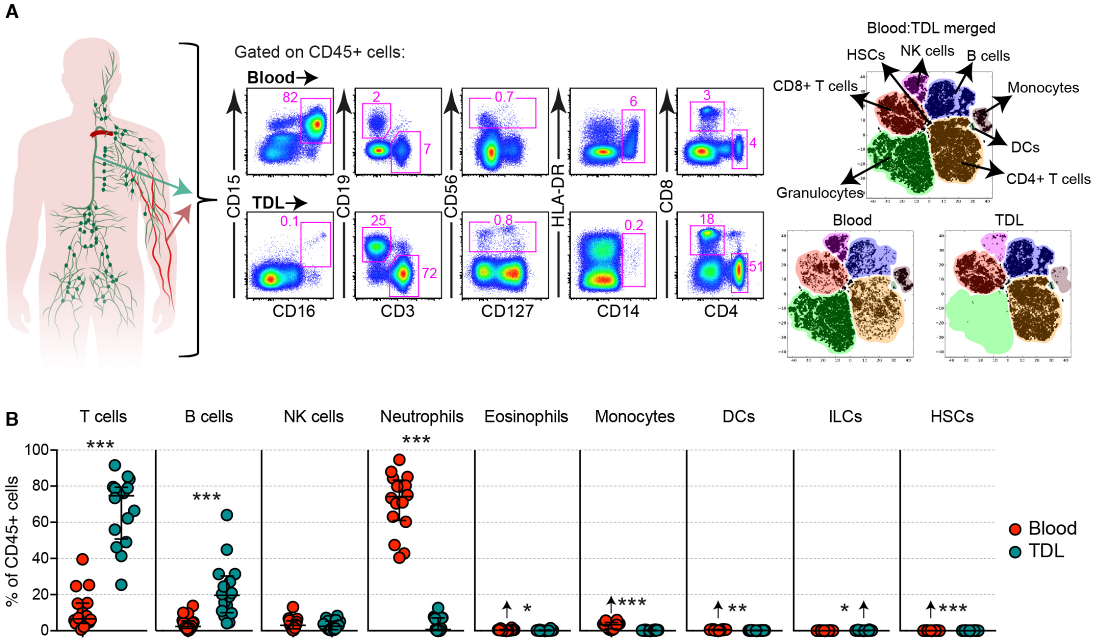

Figure 1. Immunological atlas of human TDL. (**A**) Representative flow cytometry plots with graphic (left) and merged tSNE plots (right) showing the differential immune lineage content of blood and TDL. (**B**) Quantification of immune cell subsets in matched blood and TDL. Arrows indicate higher average values. Data are shown as median ± IQR. Each dot represents one donor. *p < 0.05, **p < 0.01, ***p < 0.001. Paired t-test or Wilcoxon signed-rank test.

Figure 2

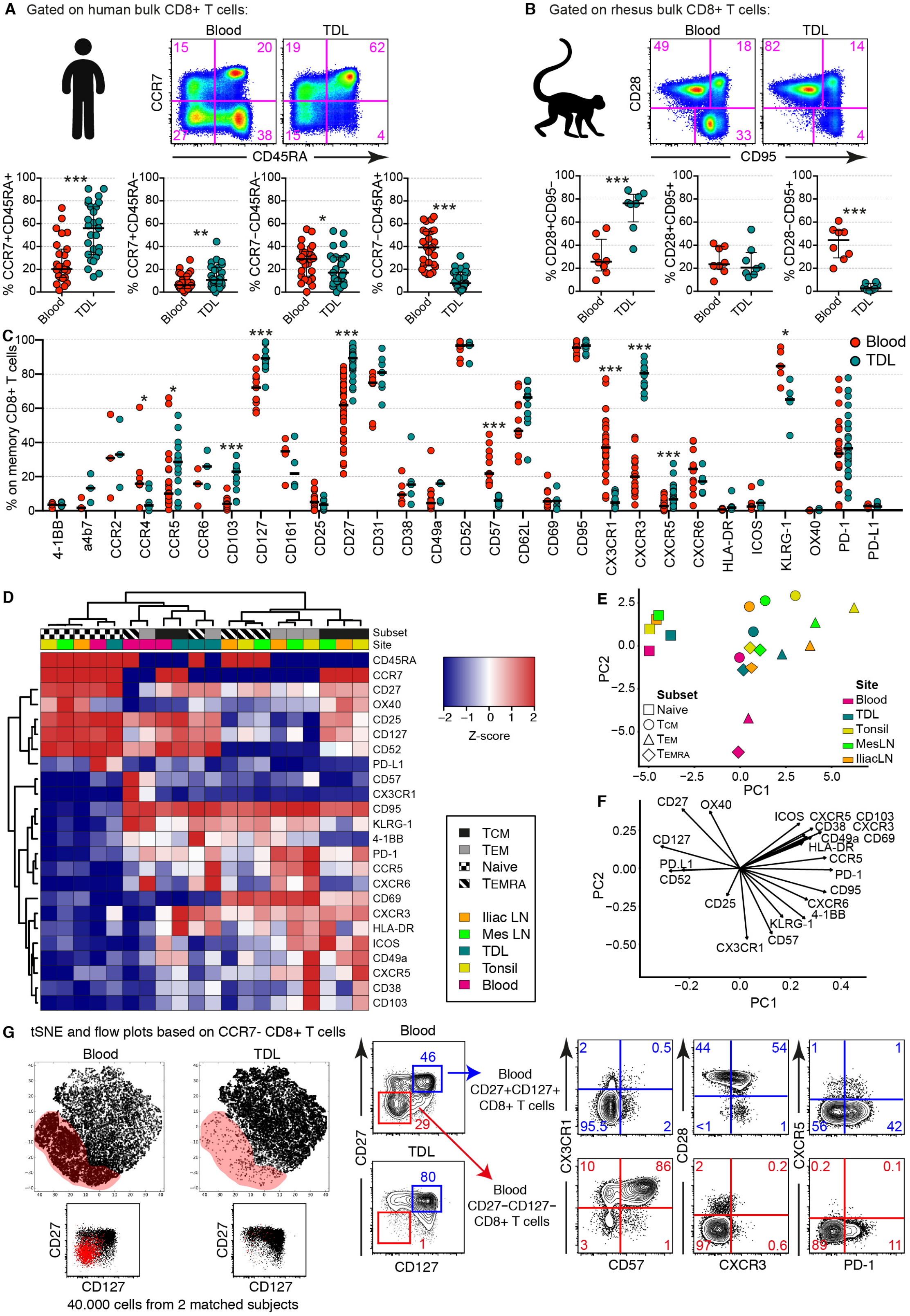

Figure 2. Highly differentiated CD8$^+$ T cells are uncommon in TDL. (**A**) Representative flow cytometry plots (top) and summary graphs (bottom) showing the frequencies of naive and memory CD8$^+$ T cell subsets in matched samples of human blood and TDL. Subsets were defined as naive (CCR7$^+$CD45RA$^+$), T$_{CM}$

($CCR7^+CD45RA^-$), T_{EM} ($CCR7^-CD45RA^-$), or T_{EMRA} ($CCR7^-CD45RA^+$). Data are shown as median ± IQR. Each dot represents one donor. *$p < 0.05$, **$p < 0.01$, ***$p < 0.001$. Paired t-test or Wilcoxon signed-rank test. (**B**) Representative flow cytometry plots (top) and summary graphs (bottom) showing the frequencies of naive and memory $CD8^+$ T cell subsets in matched samples of rhesus macaque blood and TDL. Subsets were defined as naïve ($CD28^+CD95^-$), T_{CM} ($CD28^+CD95^+$), or T_{EM} ($CD28^-CD95^+$). Data are shown as median ± IQR. Each dot represents one donor. ***$p < 0.001$. Paired t-test or Wilcoxon signed-rank test. (**C**) Expression frequencies of various markers on the surface of human memory $CD8^+$ T cells in matched samples of blood and TDL. Data are shown as median. Each dot represents one donor. *$p < 0.05$, ***$p < 0.001$. Paired t-test or Wilcoxon signed-rank test. (**D**) Heatmap showing the expression intensity of various markers on the surface of human memory $CD8^+$ T cell subsets in blood, TDL, tonsils, iliac LNs, and mesenteric LNs. Flow cytometry data are z-score-transformed in each row. (**E**) PCA plot using the dataset in (D) to show the segregation of human naive and memory $CD8^+$ T cell subsets across anatomical locations. (**F**) PCA plot showing key markers associated with the segregation observed in (E). (**G**) Merged tSNE plots (left) and flow cytometry plots (right) showing the relative absence of the $CD27^-CD127^-$ subpopulation (red) among $CCR7^-$ memory $CD8^+$ T cells in human TDL.

Figure 3

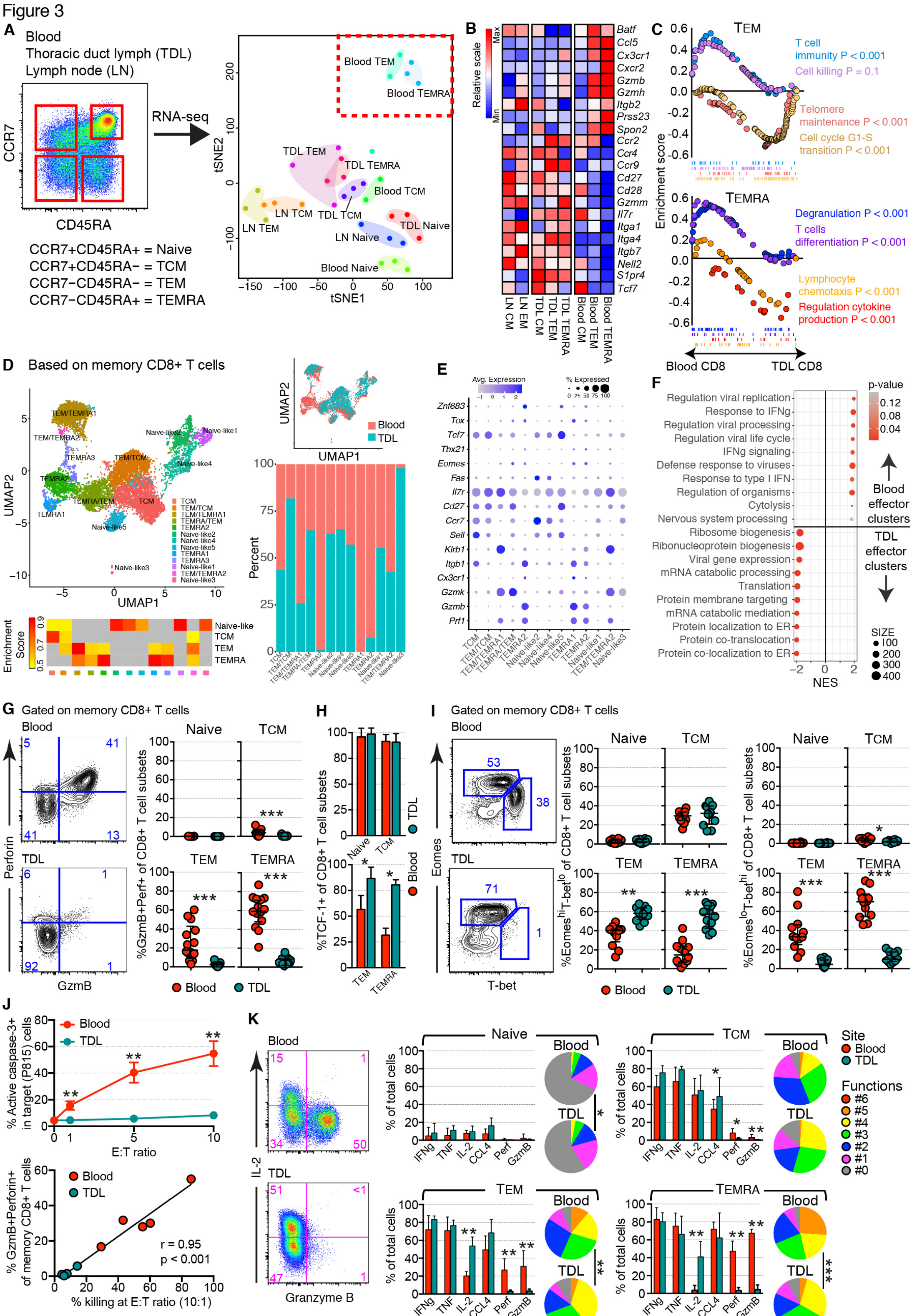

Figure 3. Effector memory CD8$^+$ cells exhibit stem-like signatures in TDL. (**A**) Representative flow cytometry plot (left) and tSNE plot (right) showing the clustering of transcriptomes from naive and memory CD8$^+$ T cell subsets in blood, TDL, and mesenteric LNs. Each dot represents one donor. (**B**) Heatmap showing the expression levels of selected genes among CD8$^+$ T$_{EM}$ and T$_{EMRA}$ cells in blood, TDL,

and mesenteric LNs. (**C**) GSEA showing the enrichment of genes associated with cytolytic activity among $CD8^+$ T_{EM} and T_{EMRA} cells in blood and the enrichment of genes associated with stemness among $CD8^+$ T_{EM} and T_{EMRA} cells in TDL. (**D**) scRNA-seq analysis of memory $CD8^+$ T cells in matched samples of blood and TDL (n = 2 donors). Left: UMAP plot illustrating the distribution of naive and memory-like clusters. The associated heatmap shows the enrichment score for each cluster according to previously reported signatures (Cano-Gamez et al., 2020). Right: UMAP plot and summary graph illustrating the distribution of memory $CD8^+$ T cells in blood (red) and TDL (blue). (**E**) Bubble plot showing the expression of selected genes. Size represents the percentage of cells in each cluster with non-zero expression of each gene, and color represents the average normalized read count for each gene in each cluster. (**F**) GSEA comparing signatures from the $CD8^+$ T_{EM}-like and T_{EMRA}-like clusters in blood and TDL versus the GO database (Broad Institute). NES, normalized enrichment score. (**G**) Representative flow cytometry plots (left) and summary graphs (right) showing the coexpression frequency of GzmB and perforin among naive and memory $CD8^+$ T cell subsets in blood and TDL. Data are shown as median ± IQR. Each dot represents one donor. ***$p < 0.001$. Unpaired t-test or Mann-Whitney *U* test. (**H**) Summary graph showing the expression frequency of TCF-1 among naive and memory $CD8^+$ T cell subsets in blood and TDL (n = 5 donors). Data are shown as median ± IQR. *$p < 0.05$. Unpaired t-test or Mann-Whitney *U* test. (**I**) Representative flow cytometry plots (left) and summary graphs (right) showing the expression frequencies of Eomes and T-bet among naive and memory $CD8^+$ T cell subsets in blood and TDL. Data are shown as median ± IQR. Each dot represents one donor. **$p < 0.01$, ***$p < 0.001$. Unpaired t-test or Mann-Whitney *U* test. (**J**) Top: cytolytic activity of $CD8^+$ T cells isolated from blood versus TDL (n = 5 donors). Redirected killing was quantified at different effector-to-target (E:T) ratios against sensitized mastocytoma cells (P815). Data are shown as median ± IQR. **$p < 0.01$. Mann-Whitney *U* test. Bottom: correlation between cytolytic activity and the coexpression frequency of GzmB and perforin among memory $CD8^+$ T cells in blood and TDL. Each dot represents one donor. Spearman rank correlation. (**K**) Representative flow cytometry plots (left) and summary graphs (right) showing chemokine/cytokine production and the upregulation GzmB and perforin among naive and memory $CD8^+$ T cell subsets in blood and TDL after stimulation with PMA and ionomycin (n = 6 donors). Data are shown as median ± IQR. *$p < 0.05$, **$p < 0.01$, ***$p < 0.001$. Unpaired t-test or Mann-Whitney *U* test. Functional profiles were compared using the permutation test in Simplified Presentation of Incredibly Complex Evaluations (SPICE).

Figure 4

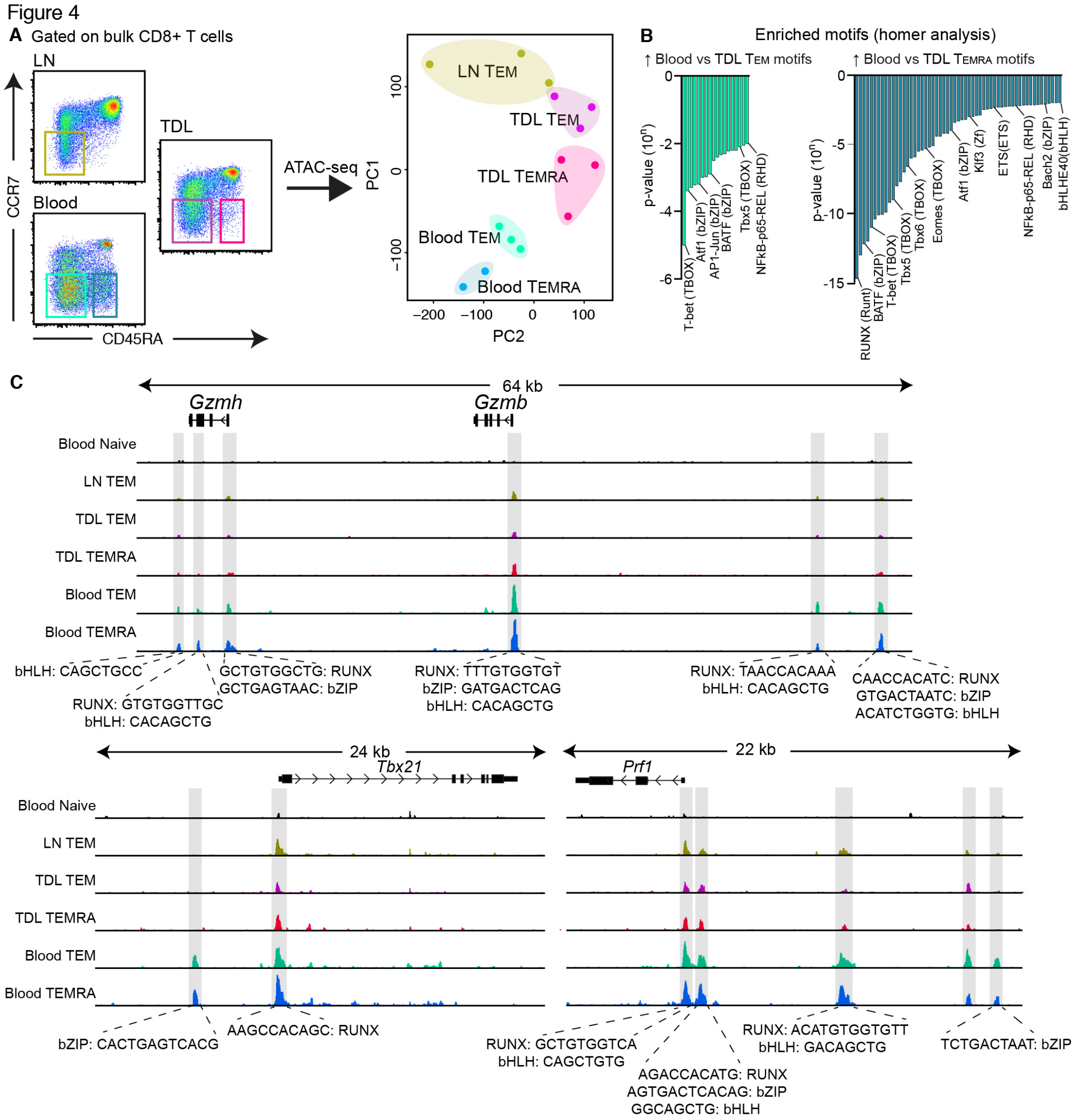

Figure 4. Effector memory CD8^{+} T cells are epigenetically distinct in blood and TDL. (**A**) Flow cytometric gating strategy for cell sorting (left) and PCA plot based on the corresponding ATAC-seq data (right) showing global chromatin accessiblity clusters for CD8^{+} T$_{EM}$ and T$_{EMRA}$ cells in blood, TDL, and mesenteric LNs. Each dot represents one donor. (**B**) Transcription factor motifs enriched among CD8^{+} T$_{EM}$ (left) and T$_{EMRA}$ cells (right) in blood versus TDL. (**C**) ATAC-seq tracks for the *Gzmh*, *Gzmb*, *Tbx21*, and *Prf1* loci among naive and memory CD8^{+} T cell subsets in blood, TDL, and mesenteric LNs.

Figure 5

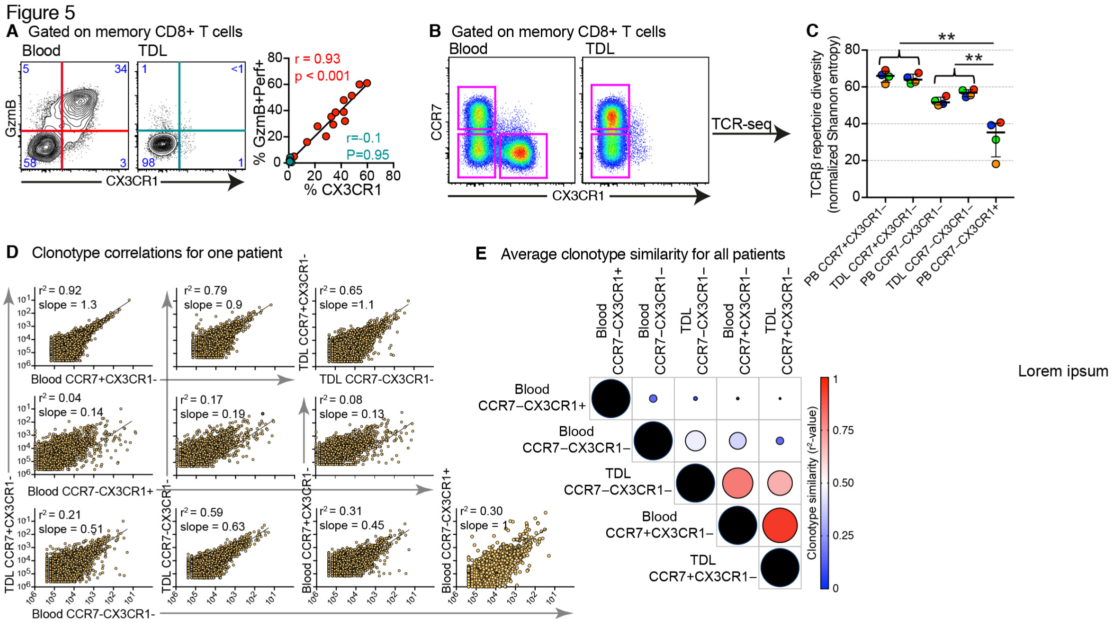

Figure 5. **Cytolytic and non-cytolytic CD8$^+$ T cells are clonotypically divergent.** (**A**) Representative flow cytometry plots (left) and scatter graph (right) showing the expression frequencies of GzmB and perforin versus CX3CR1 among memory CD8$^+$ T cells. Each dot represents one donor. Spearman rank correlation. (**B**) Flow cytometric gating strategy for sorting memory CD8$^+$ T cell subsets based on the expression of CCR7 and CX3CR1. (**C**) TCRβ repertoire diversity calculated for each memory CD8$^+$ T cell subset using normalized Shannon entropy. Data are shown as median ± IQR. Each dot represents one donor. **p < 0.01. Mann-Whitney *U* test. (**D**) Representative clonotype frequency correlations among memory CD8$^+$ T cell subsets in blood and TDL. Each dot represents one unique TCRβ sequence. (**E**) Bubble plot showing pairwise comparisons of clonotype similarity among CD8$^+$ T cell subsets in blood and TDL (n = 4 donors). (**F**) Circos plots illustrating the distribution of clonotypes among CD8$^+$ T cell subsets in blood and TDL (n = 4 donors).

Figure 6

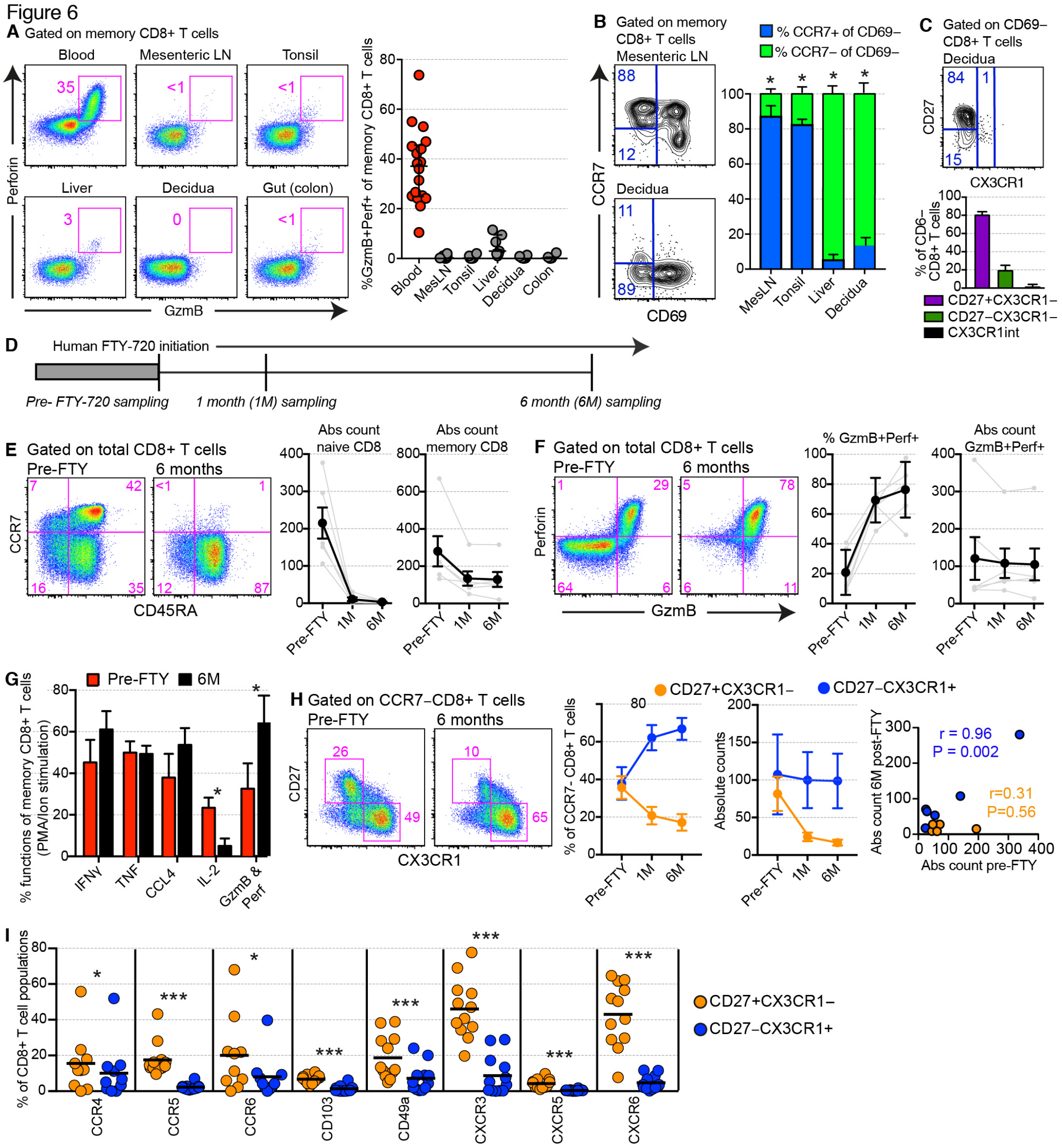

Figure 6. Cytolytic CD8$^+$ T cells are selectively retained in the intravascular circulation. (**A**) Representative flow cytometry plots (left) and summary graph (right) showing the coexpression frequencies of GzmB and perforin among memory CD8$^+$ T cells in blood, LTs, and NLTs. Data are shown as median ± IQR. Each dot represents one donor. All comparisons versus blood were highly significant. Paired t-test or Wilcoxon signed-rank test. (**B**) Representative flow cytometry plots (left) and summary graph (right) showing the expression frequencies of CCR7 and CD69 among memory CD8$^+$ T cells in LTs and NLTs (n = 15 donors). Data are shown as median ± IQR. $^*p < 0.05$. Paired t-test or Wilcoxon signed-rank test. (**C**) Representative flow cytometry plot (top) and summary graph (bottom) showing the expression frequencies of CD27 and CX3CR1 among non-resident CD8$^+$ T$_{EM}$ cells (CD69$^-$) in endometrial tissue (n = 4 donors). Data are shown as median ± IQR. (**D**) Schematic representation of the fingolimod (FTY-720) study. Blood samples were

drawn before, 1 month after (1M), and 6 months after (6M) the initiation of FTY-720. (**E**) Representative flow cytometry plots (left) and summary graphs (right) showing the frequencies (left) and absolute numbers (right) of naive and memory CD8$^+$ T cells over the course of the study. Combined data are shown as median ± IQR. Individual data are shown for each donor. (**F**) Representative flow cytometry plots (left) and summary graphs (right) showing the frequencies (left) and absolute numbers (right) of cytolytic CD8$^+$ T cells (GzmB$^+$perforin$^+$) over the course of the study. Combined data are shown as median ± IQR. Individual data are shown for each donor. (**G**) Functional profiles of memory CD8$^+$ T cells in response to stimulation with PMA and ionomycin before and 6 months after the initiation of FTY-720 ($n = 6$ donors). Data are shown as median ± IQR. *$p < 0.05$. Paired t-test or Wilcoxon signed-rank test. (**H**) Representative flow cytometry plots (left) and summary graphs (center) showing the persistence of intravascular cytolytic CD8$^+$ T cells (CCR7$^-$CD27$^-$CX3CR1$^+$) after the initiation of FTY-720 ($n = 6$ donors). Data are shown as median ± IQR. Right: correlations between the absolute numbers of intravascular cytolytic (CCR7$^-$CD27$^-$CX3CR1$^+$) and non-cytolytic CD8$^+$ T cells (CCR7$^-$CD27$^+$CX3CR1$^-$) before and 6 months after the initiation of FTY-720. Each dot represents one donor. Spearman rank correlation. (**I**) Expression frequencies of various trafficking receptors among cytolytic (CCR7$^-$CD27$^-$CX3CR1$^+$) and non-cytolytic effector memory CD8$^+$ T cells (CCR7$^-$CD27$^+$CX3CR1$^-$) in healthy donor PBMCs. Data are shown as median. Each dot represents one donor. *$p < 0.05$, ***$p < 0.001$. Paired t-test or Wilcoxon signed-rank test. NS, non-significant.

Figure 7

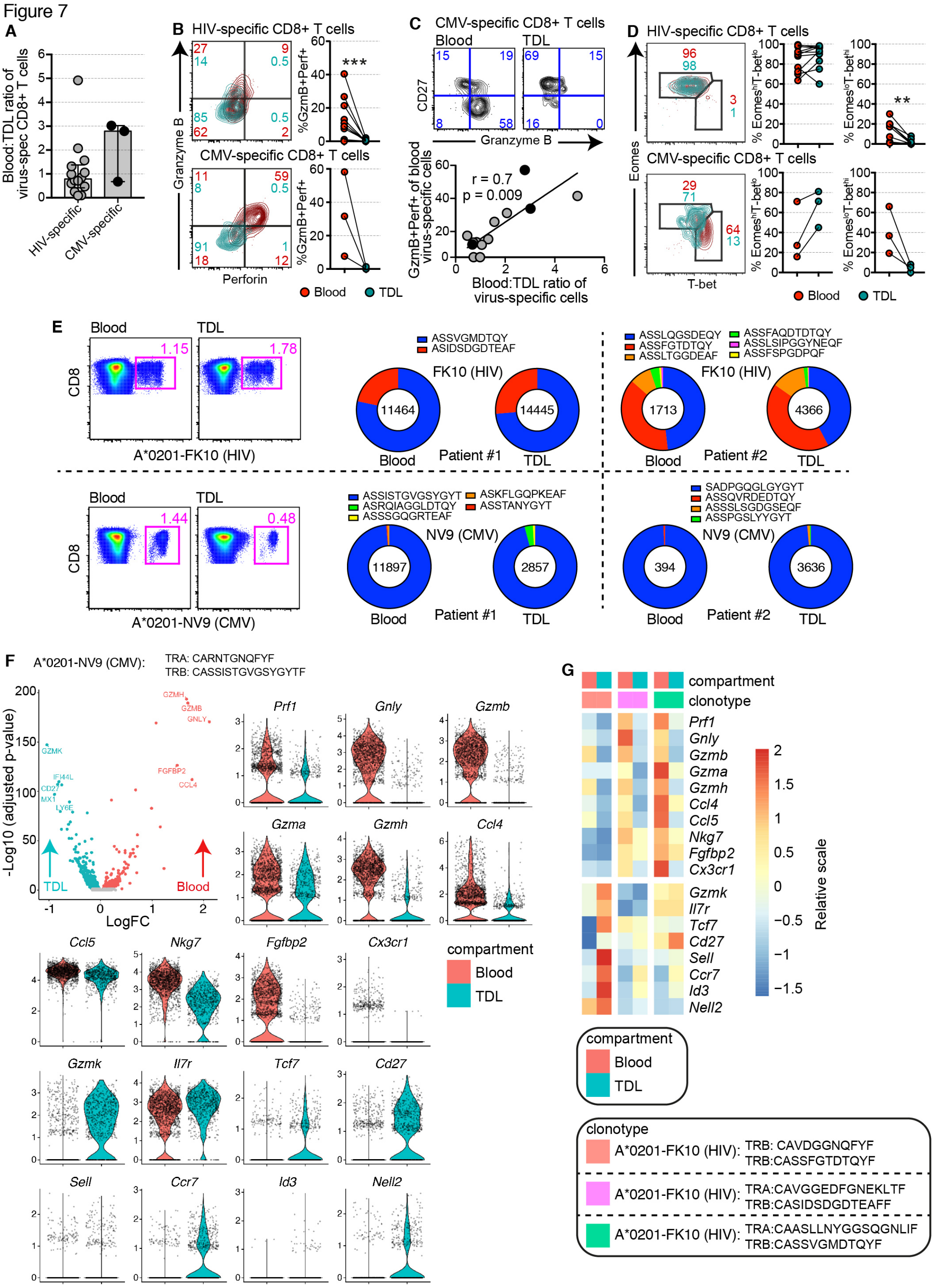

Figure 7. Virus-specific CD8$^+$ T cells rarely express cytolytic molecules in TDL. (**A**) MHC class I tetramer-based quantification of virus-specific CD8$^+$ T cells in blood and TDL (shown as ratios). Data are shown as median ± IQR. Each dot represents one specificity in one donor. (**B**) Representative flow cytometry plots (left) and summary graphs (right) showing the coexpression frequency of GzmB and perforin

among virus-specific CD8$^+$ T cells in blood and TDL. Each dot represents one specificity in one donor. ***p < 0.001. Paired t-test or Wilcoxon signed-rank test. (**C**) Top: representative flow cytometry plots showing the expression of CD27 and GzmB among CMV-specific CD8$^+$ T cells in blood and TDL. Bottom: correlation between the coexpression frequency of GzmB and perforin and the relative frequency of virus-specific CD8$^+$ T cells in blood versus TDL. Each dot represents one specificity in one donor. Spearman rank correlation. (**D**) Representative flow cytometry plots (left) and summary graphs (right) showing the expression frequencies of Eomes and T-bet among virus-specific CD8$^+$ T cells in blood and TDL. Each dot represents one specificity in one donor. **p < 0.01. Paired t-test or Wilcoxon signed-rank test. (**E**) Clonotype distribution among virus-specific CD8$^+$ T cells in blood and TDL. The number in each circle indicates the total number of sorted cells used to generate the displayed sequences. Population frequencies are shown in the corresponding flow cytometry plots (left). (**F**) Top left: volcano plots comparing single-cell gene expression for one CMV-specific CD8$^+$ T cell clonotype in blood versus TDL (n = 1 donor). Top right and bottom: violin plots showing differential expression of immune-related genes for the same CMV-specific CD8$^+$ T cell clonotype in blood versus TDL. Each dot represents one cell. (**G**) scRNA-seq heatmap showing average gene expression intensities for matched HIV-specific CD8$^+$ T cell clonotypes (n = 3) in blood versus TDL (n = 2 donors).

Figure S1

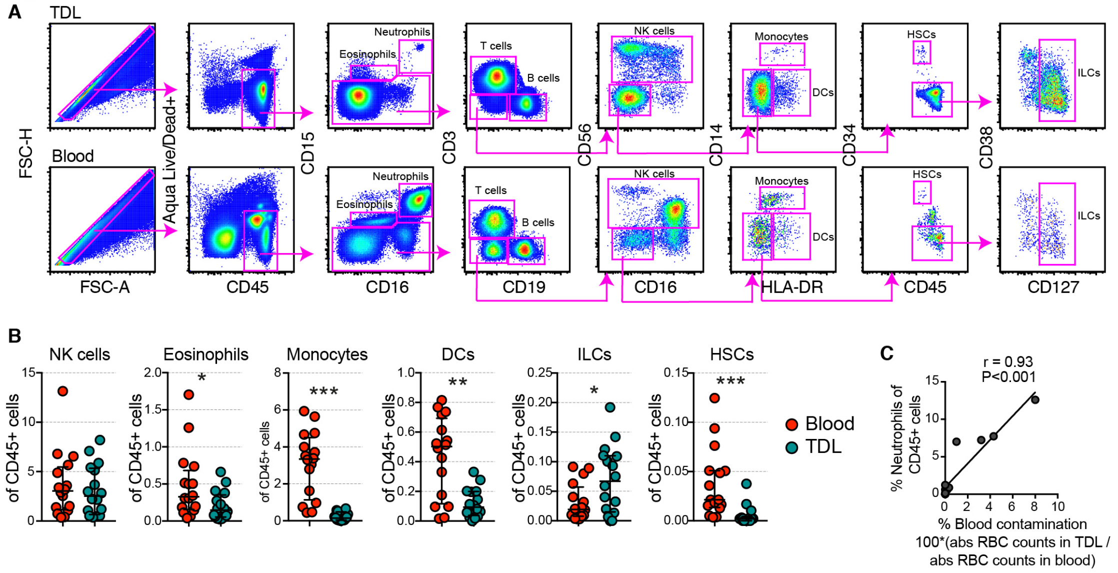

Figure S1. Flow cytometric analysis of immune cell populations in matched samples of blood and TDL. (**A**) Flow cytometric gating strategy used to identify immune lineage subsets in blood and TDL. (**B**) Quantification of immune subsets in blood versus TDL using a value-adapted y-axis. Data are shown as median ± IQR. Each dot represents one donor. *p < 0.05, **p < 0.01, ***p < 0.001. Paired t-test or Wilcoxon signed-rank test. (**C**) Correlation between the frequency of neutrophils and the relative frequency of red blood cells (RBCs) in TDL. The absolute count in TDL divided by the absolute count in blood was used to calculate the relative frequency of RBCs. Each dot represents one donor. Spearman rank correlation. Related to Figure 1.

Figure S2

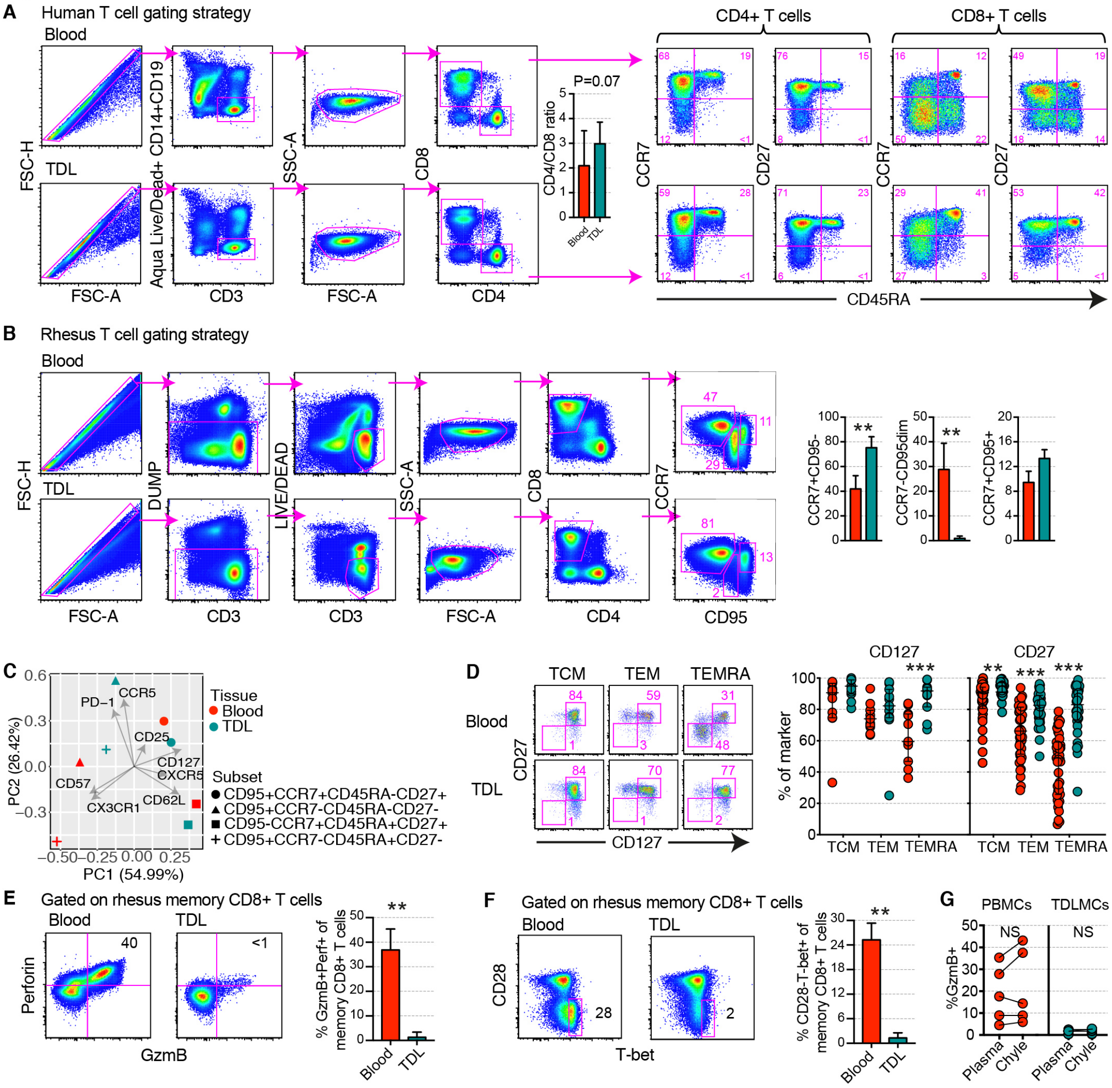

Figure S2. Flow cytometric analysis of human and rhesus macaque naive and memory CD8$^+$ T cell subsets in blood and TDL. (**A**) Flow cytometric gating strategy for the detection of human CD4$^+$ and CD8$^+$ T cell subsets in blood and TDL. The bar graph shows the overall CD4 versus CD8 ratio among CD3$^+$ cells in blood and TDL (n = 16 donors). Data are shown as median ± IQR. Mann-Whitney *U* test. (**B**) Flow cytometric gating strategy for the detection of rhesus macaque CD8$^+$ T cell subsets in blood and TDL. The bar graphs show the overall distribution of naive and memory CD8$^+$ T cell subsets based on the expression of CCR7 and CD95 (n = 8 donors). Data are shown as median ± IQR. **p < 0.01. Mann-Whitney *U* test. (**C**) PCA plot showing key markers driving the segregation of human naive and memory CD8$^+$ T cell subsets based on the expression of CD95, CCR7, CD45RA, and CD27. (**D**) Representative flow cytometry plots (left) and summary graphs (right) showing the expression frequencies of CD27 and CD127 among CD8$^+$ T$_{CM}$, T$_{EM}$, and T$_{EMRA}$ cells in blood and TDL. Data are shown as median ± IQR. Each dot represents one donor. **p < 0.01, ***p < 0.001. Mann-Whitney *U* test. (**E**) Representative flow cytometry plots (left) and summary graph (right) showing the coexpression frequency of GzmB and perforin among rhesus macaque memory CD8$^+$ T cells (non-CD28$^+$CD95$^-$) in blood and TDL (n = 8 donors). Data are shown as median ± IQR. **$p < 0.01$. Mann-Whitney *U* test. (**F**) Representative flow cytometry plots (left) and summary graph (right) showing the expression frequency of T-bet among rhesus macaque memory CD8$^+$ T cells (non-CD28$^+$CD95$^-$) in blood and TDL (n = 8 donors). Data are shown as median ± IQR. **$p < 0.01$. Mann-Whitney *U* test. **(G)** Flow cytometric quantification of GzmB among PBMCs and TDLMCs before and after incubation with matched plasma or chyle (TDL) for 5 days. Each dot represents one donor. NS, not significant. Related to Figures 2, 3, and 4.

Figure S3

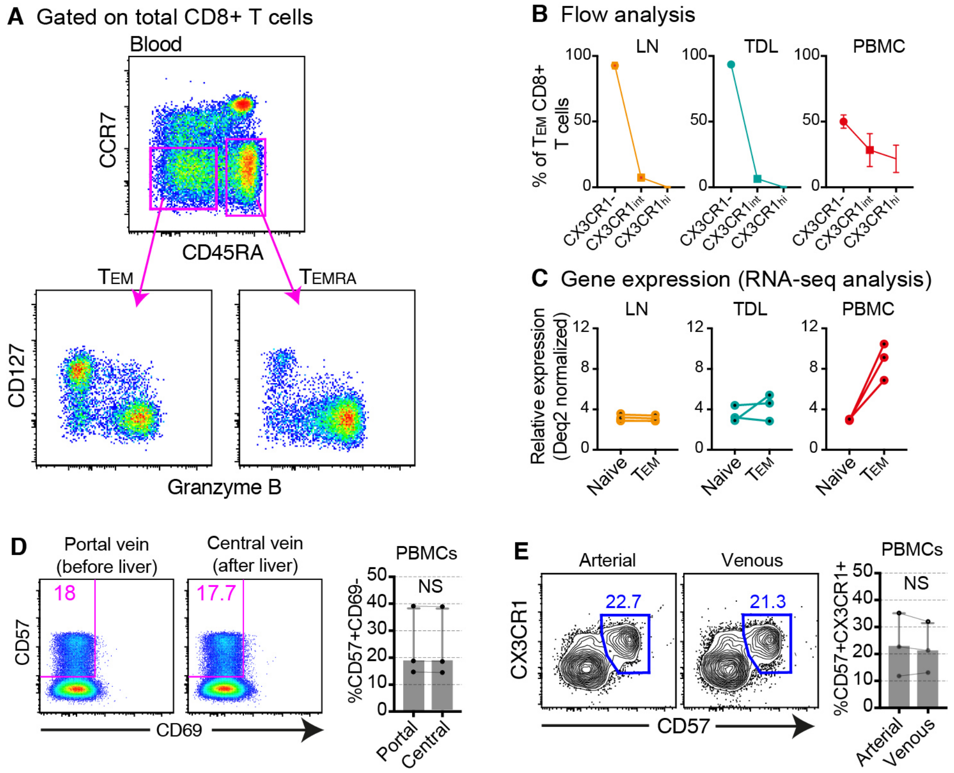

Figure S3. Flow cytometric and transcriptomic analyses of effector memory CD8$^+$ T cell subsets in blood, TDL, and mesenteric LNs. (**A**) Representative flow cytometry plots showing the expression pattern of CD127 versus GzmB among intravascular CD8$^+$ T$_{EM}$ and T$_{EMRA}$ cells. (**B**) Flow cytometric analysis showing the expression frequency of CX3CR1 among CD8$^+$ T$_{EM}$ cells in blood, TDL, and mesenteric LNs. Error bars indicate SD. (**C**) RNA-seq analysis showing relative expression of CX3CR1 among CD8$^+$ T$_{EM}$ cells in blood, TDL, and mesenteric LNs. Each dot represents one donor. (**D**) Representative flow cytometry plots (left) and summary graph (right) showing the frequencies of non-resident cytolytic CD8$^+$ T cells (CD57$^+$CD69$^-$) in the portal and central hepatic veins (n = 5 donors). Data are shown as median ± IQR. (**E**) Representative flow cytometry plots (left) and summary graph (right) showing the frequencies of non-resident cytolytic CD8$^+$ T cells (CD57$^+$CD69$^-$) in arterial and venous blood (n = 5 donors). Data are shown as median ± IQR. NS, not significant. Related to Figure 5.

Figure S4

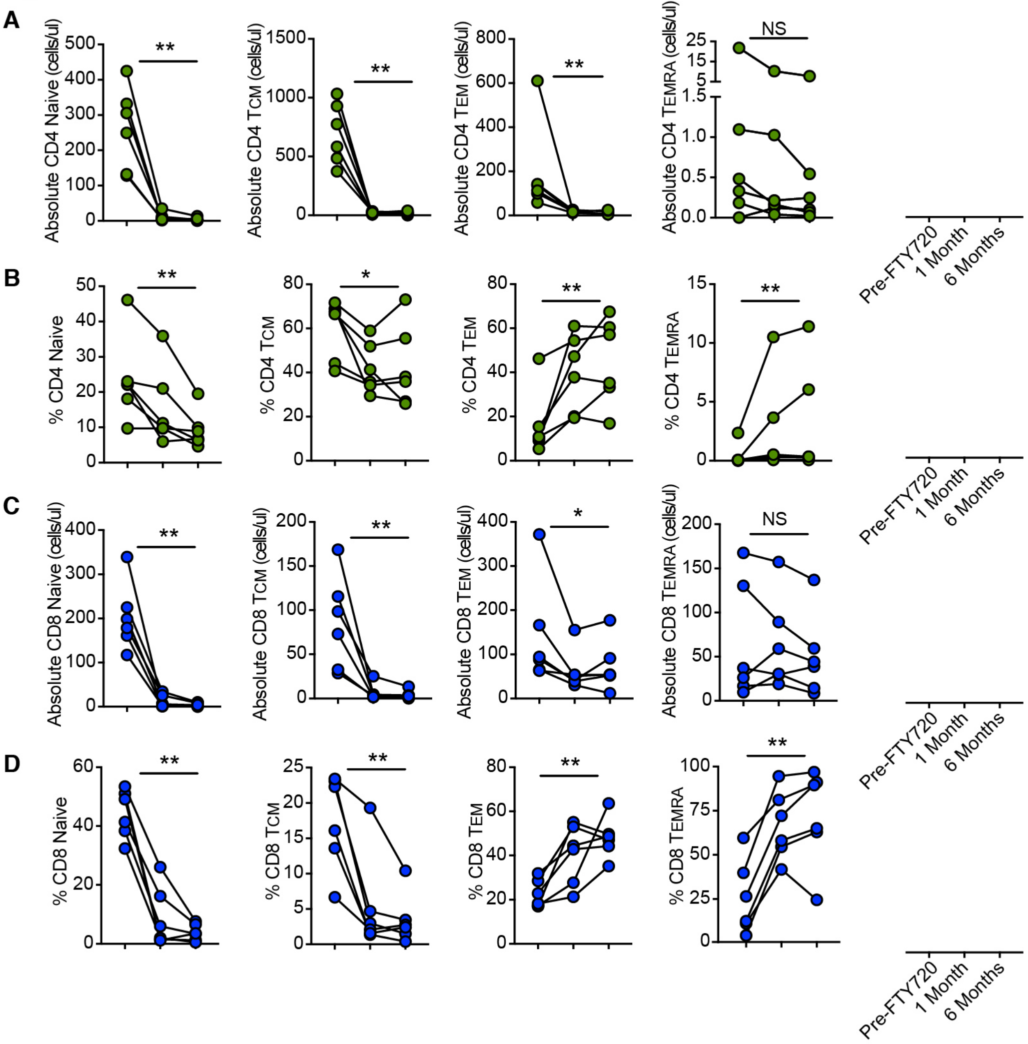

Figure S4. Global effects of FTY-720 on the intravascular T cell compartment. Before-after-graphs showing the impact of FTY-720 on naive (left), T_{CM} (center left), T_{EM} (center right), and T_{EMRA} cells (right) in the $CD4^+$ and $CD8^+$ lineages. (**A**) Absolute numbers of naive and memory $CD4^+$ T cells. (**B**) Frequencies of naive and memory $CD4^+$ T cells. (**C**) Absolute numbers of naive and memory $CD8^+$ T cells. (**D**) Frequencies of naive and memory $CD8^+$ T cells. Each dot represents one donor. *p < 0.05, **p < 0.01. Paired t-test or Wilcoxon signed-rank test. Related to Figure 6.

Figure S5

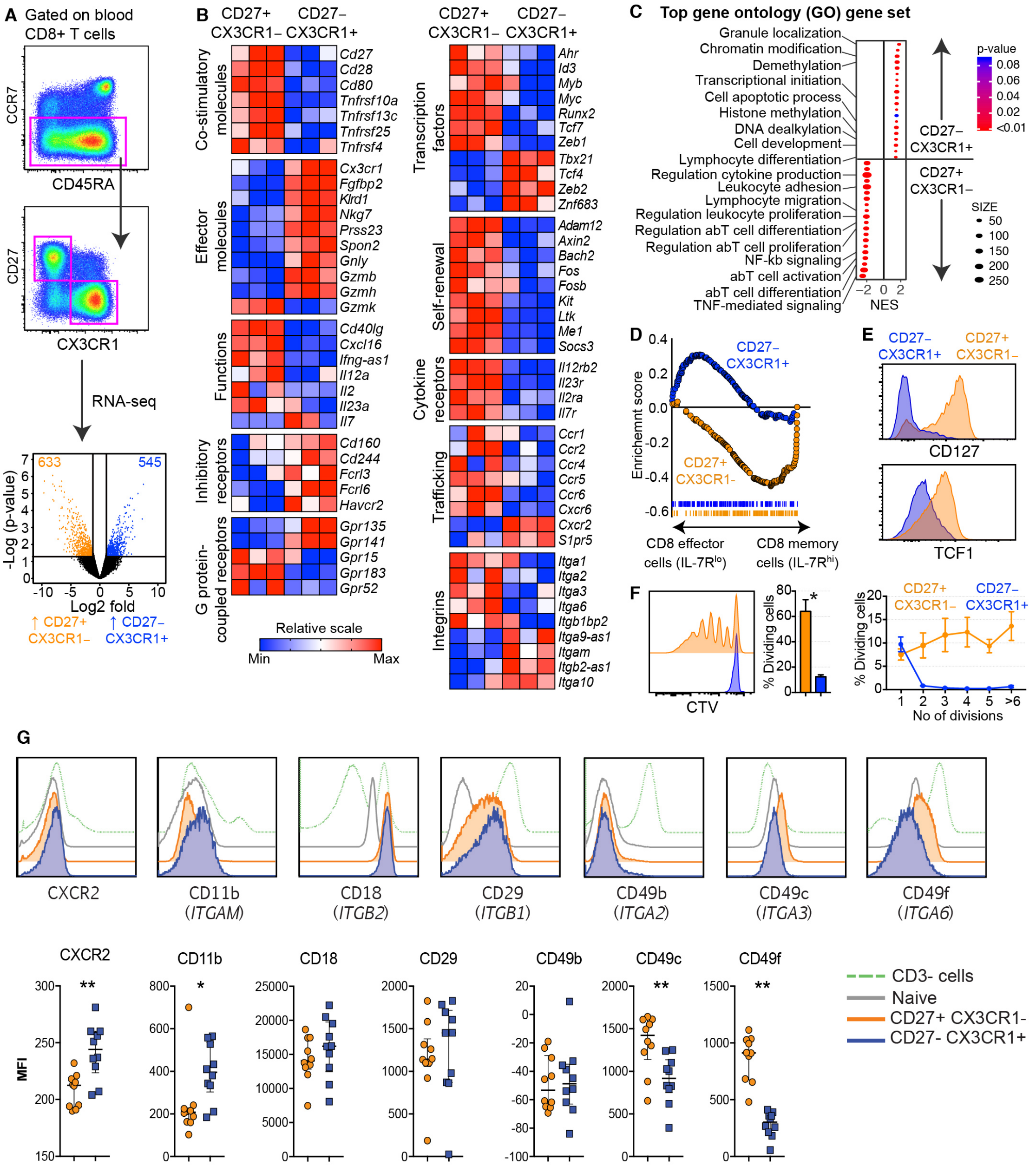

Figure S5. Cytolytic and non-cytolytic effector memory CD8$^+$ T cells are transcriptionally distinct in the intravascular circulation. (**A**) Flow cytometric gating strategy for cell sorting (top) and volcano plot (bottom) showing the number of differentially expressed genes (fold change > 2; p < 0.05) among CCR7$^-$CD27$^+$CX3CR1$^-$ versus CCR7$^-$CD27$^-$CX3CR1$^+$ memory CD8$^+$ T cells. (**B**) Heatmaps showing the differential expression of gene modules between CCR7$^-$CD27$^+$CX3CR1$^-$ and CCR7$^-$CD27$^-$CX3CR1$^+$ memory CD8$^+$ T cells. Data are z-normalized in each panel. (**C**) GSEA comparing signatures from each population versus the GO database (Broad Institute). NES, normalized enrichment score. (**D**) Enrichment analysis of memory (IL-7R^{hi}) and effector signatures (IL-7R^{lo}) among

$CCR7^-CD27^+CX3CR1^-$ and $CCR7^-CD27^-CX3CR1^+$ memory $CD8^+$ T cells. (**E**) Representative flow cytometry histograms for each population showing expression levels of CD127 and TCF-1. (**F**) Flow cytometry plot (left) and summary graphs (center and right) from a representative CellTrace Violet (CTV) dilution experiment comparing $CCR7^-CD27^+CX3CR1^-$ versus $CCR7^-CD27^-CX3CR1^+$ memory $CD8^+$ T cells. Data are shown as mean ± SD. $^*p < 0.05$. Mann-Whitney *U* test. (**G**) Representative flow cytometry histograms (top) and summary graphs (bottom) showing the expression levels of chemokine receptors and integrins that were differentially expressed among $CCR7^-CD27^+CX3CR1^-$ and $CCR7^-CD27^-CX3CR1^+$ memory $CD8^+$ T cells in the corresponding RNA-seq experiments (n = 3 donors). Data are shown as median ± IQR. Each dot represents one donor. $^*p < 0.05$, $^{**}p < 0.01$. Mann-Whitney *U* test. MFI, median fluorescence intensity. Related to Figure 6.

Figure S6

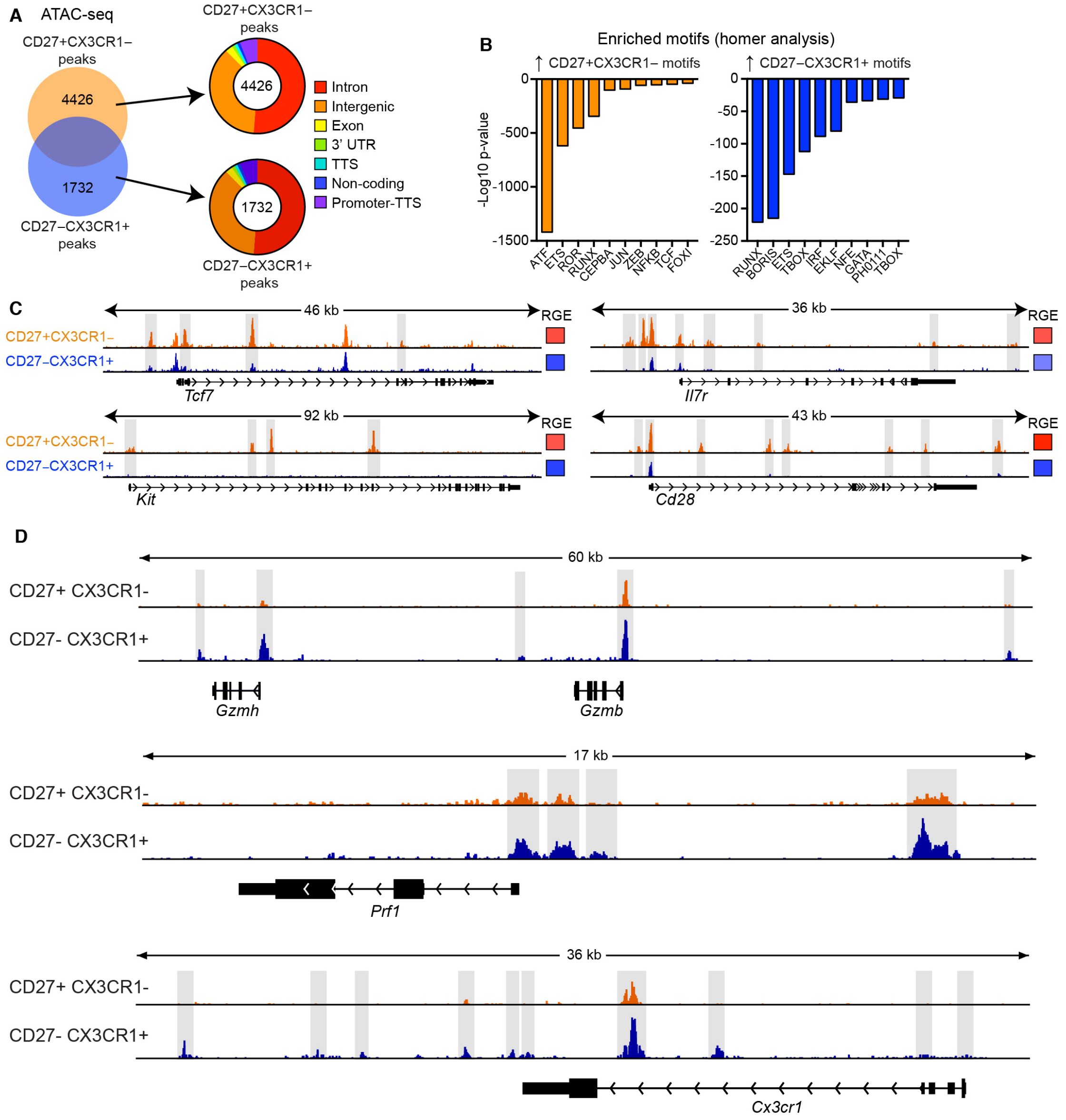

Figure S6. Epigenetic analyses of intravascular cytolytic and non-cytolytic effector memory CD8^{+} T cells. (**A**) Genomic distribution of OCRs comparing peaks from CCR7^{-}CD27^{+}CX3CR1^{-} versus CCR7^{-}CD27^{-}CX3CR1^{+} memory CD8^{+} T cells (n = 3 donors). (**B**) Bar graphs showing the enrichment of specific transcription factor binding motifs in each population (n = 3 donors). (**C**) ATAC-seq tracks demonstrating the enrichment of OCRs adjacent to *Tcf7*, *Kit*, *Il7r*, and *Cd28* among CCR7^{-}CD27^{+}CX3CR1^{-} memory CD8^{+} T cells (n = 3 donors). Heatmaps on the right show relative gene expression (RGE) from the RNA-seq analysis (blue = min; red = max). (**D**) ATAC-seq tracks for *Gzmh*, *Gzmb*, *Prf1*, and *Cx3cr1* comparing CCR7^{-}CD27^{+}CX3CR1^{-} versus CCR7^{-}CD27^{-}CX3CR1^{+} memory CD8^{+} T cells (n = 3 donors). Related to Figure 6.

Figure S7

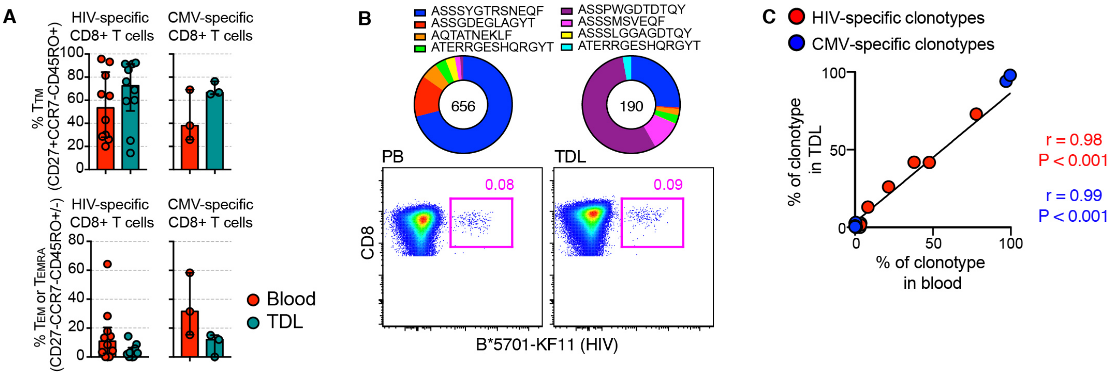

Figure S7. Anatomical distribution of virus-specific CD8^{+} T cells and clonotypes in blood versus TDL. (**A**) MHC class I tetramer-based quantification of virus-specific CD8^{+} T$_{TM}$ (top) and T$_{EM}$/T$_{EMRA}$ cells (bottom) in blood and TDL. Data are shown as median ± IQR. Each dot represents one specificity in one donor. (**B**) Clonotype distribution among a low-frequency HIV-specific CD8^{+} T cell population in blood and TDL. The number in each circle indicates the total number of sorted cells used to generate the displayed sequences. Population frequencies are shown in the corresponding flow cytometry plots (bottom). (**C**) Correlation between the frequency of virus-specific CD8^{+} T cell clonotypes in blood and the frequency of virus-specific CD8^{+} T cell clonotypes in TDL. Each dot represents a matched specificity with a minimum of 200 sorted cells per compartment. Spearman rank correlation. Related to Figure 7.

Table S1. Donor groups and clinical parameters.

HIV status	**Cohort size**	**Samples**	**Age (years)**	**Sex**	**Clinical details**
HIV$^-$	52	Matched blood and TDL	Median: 31yr IQR: 10–61yr	Male: n = 31 Female: n = 21	Idiopathic or traumatic chylopericardium, chylothorax, and/or chylous ascites
HIV$^+$	11	Matched blood and TDL	Median: 39yr IQR: 28–47yr	Male: n = 11 Female: n = 0	ART$^+$ ART$^-$ n = 8 n = 3 VL: <50 73,430 CD4: 936 416

ART, antiretroviral therapy; CD4, CD4$^+$ T cell count (cells/μL blood); VL, viral load (RNA copies/mL plasma).

REFERENCES

Appay, V., Nixon, D.F., Donahoe, S.M., Gillespie, G.M., Dong, T., King, A., Ogg, G.S., Spiegel, H.M., Conlon, C., Spina, C.A.*, et al.* (2000). HIV-specific CD8$^+$ T cells produce antiviral cytokines but are impaired in cytolytic function. J Exp Med *192*, 63–75.

Bartolome-Casado, R., Landsverk, O.J.B., Chauhan, S.K., Richter, L., Phung, D., Greiff, V., Risnes, L.F., Yao, Y., Neumann, R.S., Yaqub, S.*, et al.* (2019). Resident memory CD8 T cells persist for years in human small intestine. J Exp Med *216*, 2412–2426.

Beura, L.K., Hamilton, S.E., Bi, K., Schenkel, J.M., Odumade, O.A., Casey, K.A., Thompson, E.A., Fraser, K.A., Rosato, P.C., Filali-Mouhim, A.*, et al.* (2016). Normalizing the environment recapitulates adult human immune traits in laboratory mice. Nature *532*, 512–516.

Boritz, E.A., Darko, S., Swaszek, L., Wolf, G., Wells, D., Wu, X., Henry, A.R., Laboune, F., Hu, J., Ambrozak, D.*, et al.* (2016). Multiple origins of virus persistence during natural control of HIV infection. Cell *166*, 1004–1015.

Boschetti, G., Nancey, S., Moussata, D., Cotte, E., Francois, Y., Flourie, B., and Kaiserlian, D. (2016). Enrichment of circulating and mucosal cytotoxic CD8$^+$ T cells is associated with postoperative endoscopic recurrence in patients with Crohn's disease. J Crohns Colitis *10*, 338–345.

Bottcher, J.P., Beyer, M., Meissner, F., Abdullah, Z., Sander, J., Hochst, B., Eickhoff, S., Rieckmann, J.C., Russo, C., Bauer, T.*, et al.* (2015). Functional classification of memory CD8$^+$ T cells by CX3CR1 expression. Nat Commun *6*, 8306.

Buenrostro, J.D., Giresi, P.G., Zaba, L.C., Chang, H.Y., and Greenleaf, W.J. (2013). Transposition of native chromatin for fast and sensitive epigenomic profiling of open chromatin, DNA-binding proteins and nucleosome position. Nat Methods *10*, 1213–1218.

Buggert, M., Japp, A.S., and Betts, M.R. (2019). Everything in its right place: resident memory CD8$^+$ T cell immunosurveillance of HIV infection. Curr Opin HIV AIDS *14*, 93–99.

Buggert, M., Nguyen, S., Salgado-Montes de Oca, G., Bengsch, B., Darko, S., Ransier, A., Roberts, E.R., Del Alcazar, D., Brody, I.B., Vella, L.A.*, et al.* (2018). Identification and characterization of HIV-specific resident memory CD8$^+$ T cells in human lymphoid tissue. Sci Immunol *3*, eaar4526.

Buggert, M., Tauriainen, J., Yamamoto, T., Frederiksen, J., Ivarsson, M.A., Michaelsson, J., Lund, O., Hejdeman, B., Jansson, M., Sonnerborg, A.*, et al.* (2014). T-bet and Eomes are differentially linked to the exhausted phenotype of CD8$^+$ T cells in HIV infection. PLoS Pathog *10*, e1004251.

Cano-Gamez, E., Soskic, B., Roumeliotis, T.I., So, E., Smyth, D.J., Baldrighi, M., Wille, D., Nakic, N., Esparza-Gordillo, J., Larminie, C.G.C.*, et al.* (2020). Single-cell transcriptomics identifies an effectorness gradient shaping the response of CD4$^+$ T cells to cytokines. Nat Commun *11*, 1801.

Champagne, P., Ogg, G.S., King, A.S., Knabenhans, C., Ellefsen, K., Nobile, M., Appay, V., Rizzardi, G.P., Fleury, S., Lipp, M.*, et al.* (2001). Skewed maturation of memory HIV-specific CD8 T lymphocytes. Nature *410*, 106–111.

Duhen, T., Duhen, R., Montler, R., Moses, J., Moudgil, T., de Miranda, N.F., Goodall, C.P., Blair, T.C., Fox, B.A., McDermott, J.E.*, et al.* (2018). Co-expression of CD39 and CD103 identifies tumor-reactive CD8 T cells in human solid tumors. Nat Commun *9*, 2724.

Fong, A.M., Robinson, L.A., Steeber, D.A., Tedder, T.F., Yoshie, O., Imai, T., and Patel, D.D. (1998). Fractalkine and CX3CR1 mediate a novel mechanism of leukocyte capture, firm adhesion, and activation under physiologic flow. J Exp Med *188*, 1413–1419.

Fox, R.I., Fong, S., Tsoukas, C., and Vaughan, J.H. (1984). Characterization of recirculating lymphocytes in rheumatoid arthritis patients: selective deficiency of natural killer cells in thoracic duct lymph. J Immunol *132*, 2883–2887.

Friedman, H.M., Macarak, E.J., MacGregor, R.R., Wolfe, J., and Kefalides, N.A. (1981). Virus infection of endothelial cells. J Infect Dis *143*, 266–273.

Furze, R.C., and Rankin, S.M. (2008). Neutrophil mobilization and clearance in the bone marrow. Immunology *125*, 281–288.

Gebhardt, T., Wakim, L.M., Eidsmo, L., Reading, P.C., Heath, W.R., and Carbone, F.R. (2009). Memory T cells in nonlymphoid tissue that provide enhanced local immunity during infection with herpes simplex virus. Nat Immunol *10*, 524–530.

Gerlach, C., Moseman, E.A., Loughhead, S.M., Alvarez, D., Zwijnenburg, A.J., Waanders, L., Garg, R., de la Torre, J.C., and von Andrian, U.H. (2016). The chemokine receptor CX3CR1 defines three antigen-experienced CD8 T cell subsets with distinct roles in immune surveillance and homeostasis. Immunity *45*, 1270–1284.

Gerlach, C., Rohr, J.C., Perie, L., van Rooij, N., van Heijst, J.W., Velds, A., Urbanus, J., Naik, S.H., Jacobs, H., Beltman, J.B.*, et al.* (2013). Heterogeneous differentiation patterns of individual CD8$^+$ T cells. Science *340*, 635–639.

Gerlach, C., van Heijst, J.W., Swart, E., Sie, D., Armstrong, N., Kerkhoven, R.M., Zehn, D., Bevan, M.J., Schepers, K., and Schumacher, T.N. (2010). One naive T cell, multiple fates in CD8$^+$ T cell differentiation. J Exp Med *207*, 1235–1246.

Girardet, R.E., and Benninghoff, D.L. (1977). Long term physiologic study of thoracic duct lymph and lymphocytes in rat and man. Lymphology *10*, 36–44.

Gordon, C.L., Miron, M., Thome, J.J., Matsuoka, N., Weiner, J., Rak, M.A., Igarashi, S., Granot, T., Lerner, H., Goodrum, F., and Farber, D.L. (2017). Tissue reservoirs of antiviral T cell immunity in persistent human CMV infection. J Exp Med *214*, 651–667.

Gowans, J.L. (1957). The effect of the continuous re-infusion of lymph and lymphocytes on the output of lymphocytes from the thoracic duct of unanaesthetized rats. Br J Exp Pathol *38*, 67–78.

Gowans, J.L. (1959). The recirculation of lymphocytes from blood to lymph in the rat. J Physiol *146*, 54–69.

Gowans, J.L., and Knight, E.J. (1964). The route of re-circulation of lymphocytes in the rat. Proc R Soc Lond B Biol Sci *159*, 257–282.

Guidotti, L.G., Inverso, D., Sironi, L., Di Lucia, P., Fioravanti, J., Ganzer, L., Fiocchi, A., Vacca, M., Aiolfi, R., Sammicheli, S.*, et al.* (2015). Immunosurveillance of the liver by intravascular effector CD8$^+$ T cells. Cell *161*, 486–500.

Hall, J.G., and Morris, B. (1965). The origin of the cells in the efferent lymph from a single lymph node. J Exp Med *121*, 901–910.

Im, S.J., Hashimoto, M., Gerner, M.Y., Lee, J., Kissick, H.T., Burger, M.C., Shan, Q., Hale, J.S., Lee, J., Nasti, T.H.*, et al.* (2016). Defining CD8$^+$ T cells that provide the proliferative burst after PD-1 therapy. Nature *537*, 417–421.

Imai, T., Hieshima, K., Haskell, C., Baba, M., Nagira, M., Nishimura, M., Kakizaki, M., Takagi, S., Nomiyama, H., Schall, T.J., and Yoshie, O. (1997). Identification and molecular characterization of fractalkine receptor CX3CR1, which mediates both leukocyte migration and adhesion. Cell *91*, 521–530.

Jarvis, M.A., and Nelson, J.A. (2007). Human cytomegalovirus tropism for endothelial cells: not all endothelial cells are created equal. J Virol *81*, 2095–2101.

Jeannet, G., Boudousquie, C., Gardiol, N., Kang, J., Huelsken, J., and Held, W. (2010). Essential role of the Wnt pathway effector Tcf-1 for the establishment of functional CD8 T cell memory. Proc Natl Acad Sci U S A *107*, 9777–9782.

Klicznik, M.M., Morawski, P.A., Hollbacher, B., Varkhande, S.R., Motley, S.J., Kuri-Cervantes, L., Goodwin, E., Rosenblum, M.D., Long, S.A., Brachtl, G., *et al.* (2019). Human $CD4^{+}CD103^{+}$ cutaneous resident memory T cells are found in the circulation of healthy individuals. Sci Immunol *4*, eaav8995.

Kubik, S. (1973). Anatomy of the lymphatic system. Radiol Clin Biol *42*, 243–257.

Kumar, B.V., Ma, W., Miron, M., Granot, T., Guyer, R.S., Carpenter, D.J., Senda, T., Sun, X., Ho, S.H., Lerner, H., *et al.* (2017). Human tissue-resident memory T cells are defined by core transcriptional and functional signatures in lymphoid and mucosal sites. Cell Rep *20*, 2921–2934.

Lemaire, L.C., van Deventer, S.J., van Lanschot, J.J., Meenan, J., and Gouma, D.J. (1998). Phenotypical characterization of cells in the thoracic duct of patients with and without systemic inflammatory response syndrome and multiple organ failure. Scand J Immunol *47*, 69–75.

Mackay, C.R., Andrew, D.P., Briskin, M., Ringler, D.J., and Butcher, E.C. (1996). Phenotype, and migration properties of three major subsets of tissue homing T cells in sheep. Eur J Immunol *26*, 2433–2439.

Mackay, C.R., Kimpton, W.G., Brandon, M.R., and Cahill, R.N. (1988). Lymphocyte subsets show marked differences in their distribution between blood and the afferent and efferent lymph of peripheral lymph nodes. J Exp Med *167*, 1755–1765.

Mackay, C.R., Marston, W.L., and Dudler, L. (1990). Naive and memory T cells show distinct pathways of lymphocyte recirculation. J Exp Med *171*, 801–817.

Mackay, C.R., Marston, W.L., Dudler, L., Spertini, O., Tedder, T.F., and Hein, W.R. (1992). Tissue-specific migration pathways by phenotypically distinct subpopulations of memory T cells. Eur J Immunol *22*, 887–895.

Maddox, J.F., Mackay, C.R., and Brandon, M.R. (1985). Surface antigens, SBU-T4 and SBU-T8, of sheep T lymphocyte subsets defined by monoclonal antibodies. Immunology *55*, 739–748.

Masopust, D., Choo, D., Vezys, V., Wherry, E.J., Duraiswamy, J., Akondy, R., Wang, J., Casey, K.A., Barber, D.L., Kawamura, K.S., *et al.* (2010). Dynamic T cell migration program provides resident memory within intestinal epithelium. J Exp Med *207*, 553–564.

Masopust, D., Vezys, V., Marzo, A.L., and Lefrancois, L. (2001). Preferential localization of effector memory cells in nonlymphoid tissue. Science *291*, 2413–2417.

Masopust, D., Vezys, V., Wherry, E.J., Barber, D.L., and Ahmed, R. (2006). Cutting edge: gut microenvironment promotes differentiation of a unique memory CD8 T cell population. J Immunol *176*, 2079–2083.

McLane, L.M., Banerjee, P.P., Cosma, G.L., Makedonas, G., Wherry, E.J., Orange, J.S., and Betts, M.R. (2013). Differential localization of T-bet and Eomes in CD8 T cell memory populations. J Immunol *190*, 3207–3215.

Miller, J.F., and Sprent, J. (1971). Thymus-derived cells in mouse thoracic duct lymph. Nat New Biol *230*, 267–270.

Nadolski, G.J., and Itkin, M. (2012). Feasibility of ultrasound-guided intranodal lymphangiogram for thoracic duct embolization. J Vasc Interv Radiol *23*, 613–616.

Nguyen, S., Deleage, C., Darko, S., Ransier, A., Truong, D.P., Agarwal, D., Japp, A.S., Wu, V.H., Kuri-Cervantes, L., Abdel-Mohsen, M., *et al.* (2019). Elite control of

HIV is associated with distinct functional and transcriptional signatures in lymphoid tissue CD8$^+$ T cells. Sci Transl Med *11*, eaax4077.

Pabst, R. (1988). The spleen in lymphocyte migration. Immunol Today *9*, 43–45.

Pallett, L.J., Davies, J., Colbeck, E.J., Robertson, F., Hansi, N., Easom, N.J.W., Burton, A.R., Stegmann, K.A., Schurich, A., Swadling, L.*, et al.* (2017). IL-2^{high} tissue-resident T cells in the human liver: sentinels for hepatotropic infection. J Exp Med *214*, 1567–1580.

Patil, V.S., Madrigal, A., Schmiedel, B.J., Clarke, J., O'Rourke, P., de Silva, A.D., Harris, E., Peters, B., Seumois, G., Weiskopf, D.*, et al.* (2018). Precursors of human CD4$^+$ cytotoxic T lymphocytes identified by single-cell transcriptome analysis. Sci Immunol *3*, eaan8664.

Phang, K., Bowman, M., Phillips, A., and Windsor, J. (2014). Review of thoracic duct anatomical variations and clinical implications. Clin Anat *27*, 637–644.

Price, D.A., Brenchley, J.M., Ruff, L.E., Betts, M.R., Hill, B.J., Roederer, M., Koup, R.A., Migueles, S.A., Gostick, E., Wooldridge, L.*, et al.* (2005). Avidity for antigen shapes clonal dominance in CD8$^+$ T cell populations specific for persistent DNA viruses. J Exp Med *202*, 1349–1361.

Reuter, M.A., Del Rio Estrada, P.M., Buggert, M., Petrovas, C., Ferrando-Martinez, S., Nguyen, S., Sada Japp, A., Ablanedo-Terrazas, Y., Rivero-Arrieta, A., Kuri-Cervantes, L.*, et al.* (2017). HIV-specific CD8$^+$ T cells exhibit reduced and differentially regulated cytolytic activity in lymphoid tissue. Cell Rep *21*, 3458–3470.

Roberts, E.R., Carnathan, D.G., Li, H., Shaw, G.M., Silvestri, G., and Betts, M.R. (2016). Collapse of cytolytic potential in SIV-specific CD8$^+$ T cells following acute SIV infection in rhesus macaques. PLoS Pathog *12*, e1006135.

Sallusto, F., Lenig, D., Forster, R., Lipp, M., and Lanzavecchia, A. (1999). Two subsets of memory T lymphocytes with distinct homing potentials and effector functions. Nature *401*, 708–712.

Sathaliyawala, T., Kubota, M., Yudanin, N., Turner, D., Camp, P., Thome, J.J., Bickham, K.L., Lerner, H., Goldstein, M., Sykes, M.*, et al.* (2013). Distribution and compartmentalization of human circulating and tissue-resident memory T cell subsets. Immunity *38*, 187–197.

Schenkel, J.M., Fraser, K.A., Vezys, V., and Masopust, D. (2013). Sensing and alarm function of resident memory CD8$^+$ T cells. Nat Immunol *14*, 509–513.

Schick, P., Trepel, F., Lehmann-Brockhaus, E., and Nietmann, H. (1975). Autotransufsion of ^{3}H-cytidine-labelled blood lymphocytes in patients with Hodgkin's disease and non-Hodgkin patients. I. Limitations of the method. Acta Haematol *53*, 193–205.

Schulz, C., Schafer, A., Stolla, M., Kerstan, S., Lorenz, M., von Bruhl, M.L., Schiemann, M., Bauersachs, J., Gloe, T., Busch, D.H.*, et al.* (2007). Chemokine fractalkine mediates leukocyte recruitment to inflammatory endothelial cells in flowing whole blood: a critical role for P-selectin expressed on activated platelets. Circulation *116*, 764–773.

Siddiqui, I., Schaeuble, K., Chennupati, V., Fuertes Marraco, S.A., Calderon-Copete, S., Pais Ferreira, D., Carmona, S.J., Scarpellino, L., Gfeller, D., Pradervand, S.*, et al.* (2019). Intratumoral Tcf1$^+$PD-1$^+$CD8$^+$ T cells with stem-like properties promote tumor control in response to vaccination and checkpoint blockade immunotherapy. Immunity *50*, 195–211 e110.

Smith, J.B., McIntosh, G.H., and Morris, B. (1970). The traffic of cells through tissues: a study of peripheral lymph in sheep. J Anat *107*, 87–100.

Sprent, J. (1973). Circulating T and B lymphocytes of the mouse. I. Migratory properties. Cell Immunol *7*, 10–39.

Steinert, E.M., Schenkel, J.M., Fraser, K.A., Beura, L.K., Manlove, L.S., Igyarto, B.Z., Southern, P.J., and Masopust, D. (2015). Quantifying memory CD8 T cells reveals regionalization of immunosurveillance. Cell *161*, 737–749.

Strioga, M., Pasukoniene, V., and Characiejus, D. (2011). $CD8^+$ $CD28^-$ and $CD8^+$ $CD57^+$ T cells and their role in health and disease. Immunology *134*, 17–32.

Szabo, P.A., Miron, M., and Farber, D.L. (2019). Location, location, location: tissue resident memory T cells in mice and humans. Sci Immunol *4*, eaas9673.

Utzschneider, D.T., Charmoy, M., Chennupati, V., Pousse, L., Ferreira, D.P., Calderon-Copete, S., Danilo, M., Alfei, F., Hofmann, M., Wieland, D., *et al.* (2016). T cell factor 1-expressing memory-like $CD8^+$ T cells sustain the immune response to chronic viral infections. Immunity *45*, 415–427.

Valbuena, G., and Walker, D.H. (2006). The endothelium as a target for infections. Annu Rev Pathol *1*, 171–198.

Vella, L.A., Buggert, M., Manne, S., Herati, R.S., Sayin, I., Kuri-Cervantes, L., Bukh Brody, I., O'Boyle, K.C., Kaprielian, H., Giles, J.R., *et al.* (2019). T follicular helper cells in human efferent lymph retain lymphoid characteristics. J Clin Invest *130*, 3185–3200.

Voillet, V., Buggert, M., Slichter, C.K., Berkson, J.D., Mair, F., Addison, M.M., Dori, Y., Nadolski, G., Itkin, M.G., Gottardo, R., *et al.* (2018). Human MAIT cells exit peripheral tissues and recirculate via lymph in steady state conditions. JCI Insight *3*, 98487.

Wakim, L.M., Waithman, J., van Rooijen, N., Heath, W.R., and Carbone, F.R. (2008). Dendritic cell-induced memory T cell activation in nonlymphoid tissues. Science *319*, 198–202.

Zhao, Y., Zou, W., Du, J., and Zhao, Y. (2018). The origins and homeostasis of monocytes and tissue-resident macrophages in physiological situation. J Cell Physiol *233*, 6425–6439.

Zhou, X., Yu, S., Zhao, D.M., Harty, J.T., Badovinac, V.P., and Xue, H.H. (2010). Differentiation and persistence of memory $CD8^+$ T cells depend on T cell factor 1. Immunity *33*, 229–240.